Product Development Team
for
Advanced Weather Radar Techniques
Quarterly Report – 2nd Quarter FY 06

06.6.19 Common Radar Data Acquisition Techniques for FAA Radars (WSR-88D, TDWR, ASR-9)

Traditionally, algorithm techniques are developed for the radar product generator. This approach limits the algorithms to utilize data after its collection at the radar. Developing techniques for use on the data collected at its origin and in its native forms allows for new approaches to address FAA needs across multiple radar platforms.

a) Current Efforts

We have begun our collaboration with NSSL to collect I&Q data with the KOUN NEXRAD. Alternate transmission of multi-PRI and phase-coded scans will allow comparison of range-velocity ambiguity mitigation performance for various weather types. Specific pulse and phase sequences will be coded and new VCPs generated for this task. We plan to start data collection in June 2006.

b) Planned Efforts

Perform R-V ambiguity mitigation comparison with collected data. Collect sufficient data sets for comparison as needed contingent on available radar time.

c) Problems/Issues

None.

d) Interface with other Organizations

None.

e) Activity Schedule Changes

None.

06.6.22   Polarimetric Mixed-Phase Cloud Identification

Polarimetric radar measurements are sensitive to hydrometeor types and mixed-phase precipitation in particular. The measurements have potential for icing detection and for determining regions within storms in which hazardous icing conditions are likely to exist. The measurements may also have benefits for designating regions within storms where the probability of icing is low.

<u>a) Current Efforts</u>

NSSL

1. New classification algorithm. General description

The major thrust of the FAA-related dual-polarization research at NSSL in the last quarter was on substantial modification of the polarimetric classification algorithm. In the past, two separate versions of the polarimetric classifier were utilized: one for "warm season" and another for "cold season". The former one didn't attempt to classify mixed-phase and frozen categories of hydrometeors. However, it demonstrated very good skills in separating meteorological and nonmeteorological echoes and in hail detection.

A new classification algorithm is designed to distinguish between 10 classes of radar echo: (1) Ground clutter / anomalous propagation (GC/AP), (2) biological scatterers (BS), (3) dry aggregated snow (DS), (4) wet snow (WS), (5) crystals (CR), (6) graupel (GR), (7) "big drops" (BD), (8) light and moderate rain (RA), (9) heavy rain (HR), and (10) hail (HA). A whole suite of six radar variables is used for discrimination: radar reflectivity Z, differential reflectivity Z_{DR}, specific differential phase K_{DP}, cross-correlation coefficient ρ_{hv}, the texture parameters of Z (SD(Z)) and total differential phase ϕ_{DP}.

Four following novelties are incorporated in the new version of the classification algorithm:
(1) Fuzzy logic procedure is preceded by and contingent on the melting layer detection.
(2) Each radar variable is supplemented with its quality index Q_j
(3) A matrix of weights W_{ij} depending on a particular variable and class is introduced
(4) Aggregation score Ai for each class is determined as

$$A_i = \frac{\sum\limits_{j=1}^{6} W_{ij} Q_j P^{(i)}(V_j)}{\sum\limits_{j=1}^{6} W_{ij} Q_j}, \quad i = 1, \ldots, 10. \tag{1}$$

In (1), $P^{(i)}(V_j)$ is a membership function for radar variable V_j and ith class.

For each pixel or gate, every radar variable is supplemented with its quality index Qj depending on its vulnerability to (a) attenuation, (b) nonuniform beam filling effects,(c) magnitude of ?hv that characterizes statistical measurement errors for all polarimetric variables, and (d) signal-to-noise ratio SNR. The quality index decreases as severity of any of the four mentioned factors increases, thus lower weight is automatically given to the variable with lower confidence factor.

The matrix of weights W characterizes the importance or rank of each variable with respect to identification of a particular class. For example, for biological scatterers ρ_{hv} has highest rank followed by the texture parameters of Z and ϕ_{DP} with the other three radar variables lagging behind. In the case of rain, however, Z is the most important variable followed by KDP with other variables having lesser weights.

The procedure for polarimetric melting detection was described in previous reports. It proved to be quite robust and reliable as comparisons of radar designations with the output of the RUC model and results of soundings indicate.

2. Testing and evaluation: First results.

The new scheme was tested on a number of cases. So far we validated it using criteria of spatial and temporal continuity as well as consistency with simple physical considerations, e.g., graupel / hail is expected at midleveles in convective cells whereas stratiform rain is likely associated with wet and dry aggregated snow aloft.

Figs. 1 - 4 illustrate PPI fields of Z, Z_{DR}, and ρ_{hv} measured with KOUN radar as well as results of classification for the case of mesoscale convective system observed on May 13, 2005 in central Oklahoma. The data are presented in the WDSS format which will be used by the majority of operational users.

The classification algorithm correctly recognized all important features in different areas of radar echo including gust front ahead of the squall line, hail and graupel in the convective (southern) flank of the storm, rain - wet snow - dry
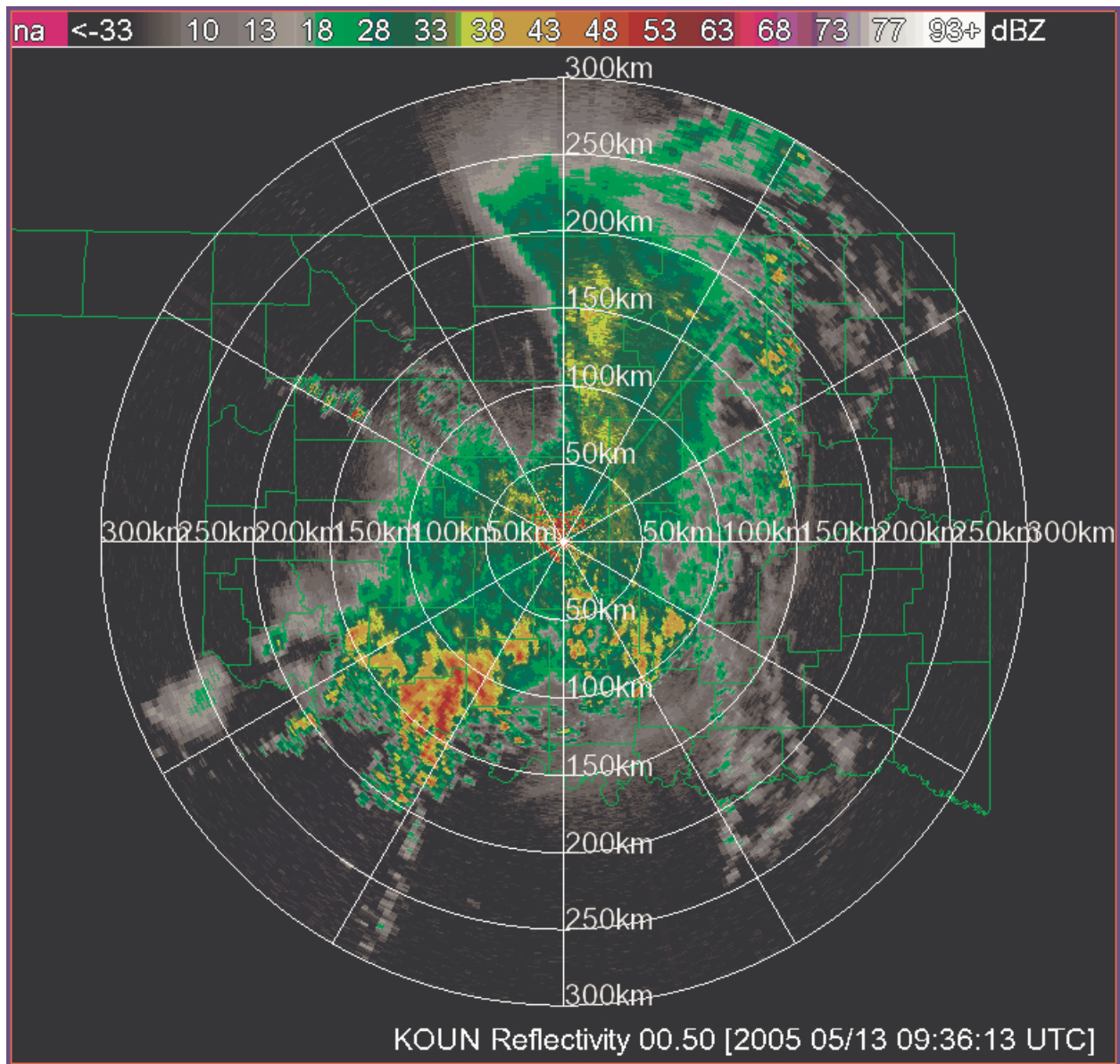
Figure 1. PPI of radar reflectivity.

snow - crystals gradual transition in the stratiform (northern) flank of the MCS, and anomalous propagation echoes behind the storms due to outflow of cold and moist air.

Another example showing a composite plot of Z, Z_{DR}, ρ_{hv}, and results of classification for the same storm but different time is illustrated in Fig. 5.

All presented images demonstrated very well superb classification capability of the new polarimetric scheme in the situations where the radar echoes from liquid, mixed-phase, and frozen hydrometeors coexist with radar returns from ground and biological targets.
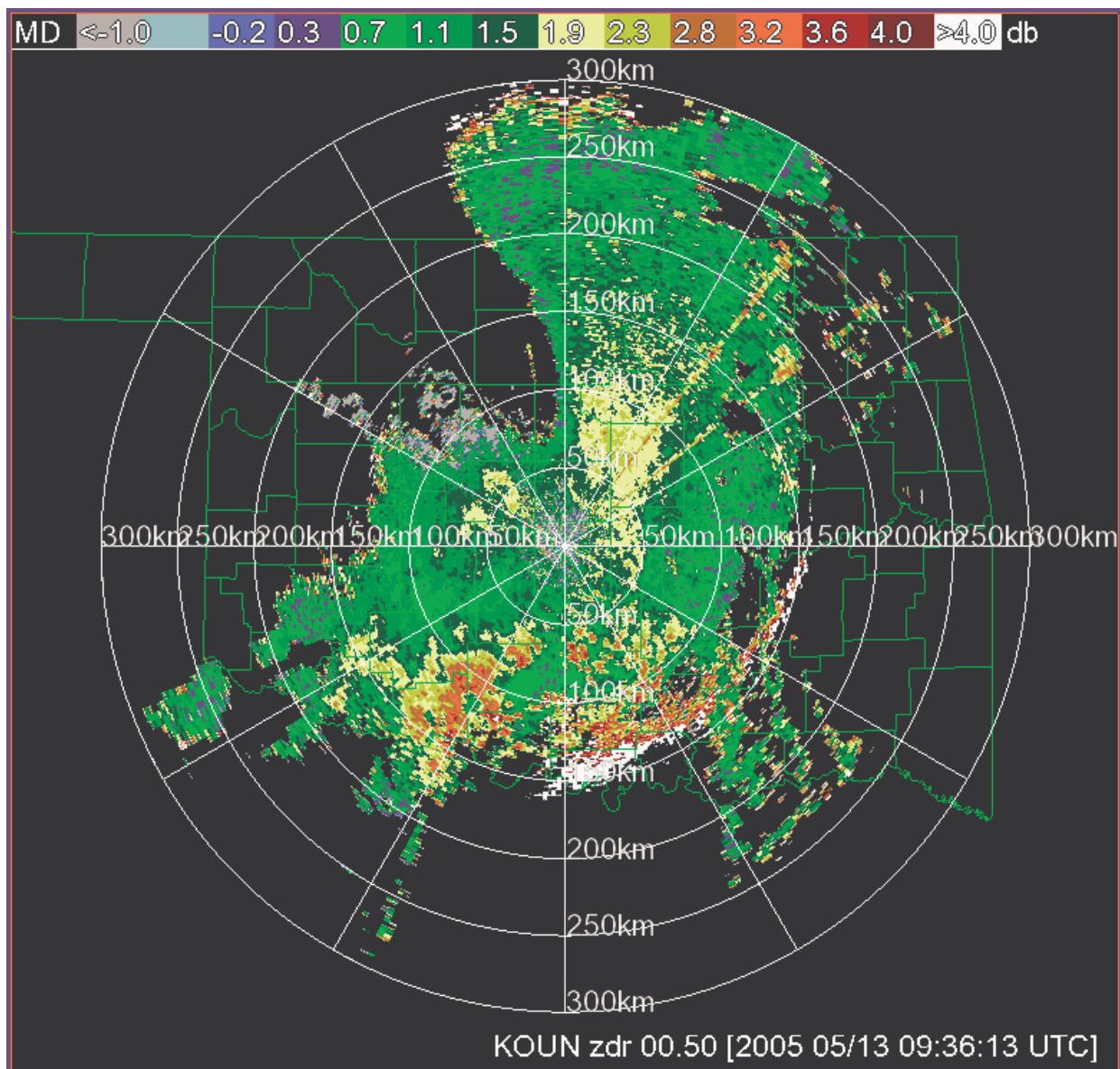
Figure 2. PPI of differential reflectivity.

NCAR

The development of a high-resolution radar-based icing product that combines components of the Current Icing Potential (CIP) algorithm of the In-Flight Icing PDT, the Freezing Level Algorithm (FLA), meteorological observations, numerical forecasts, and the NCAR Hydrometeor Classification Algorithm (HCA), is progressing. [A draft development plan is attached as Appendix 1.] Icing events from the IMPROVE and MAP field programs are being examined for development purposes.

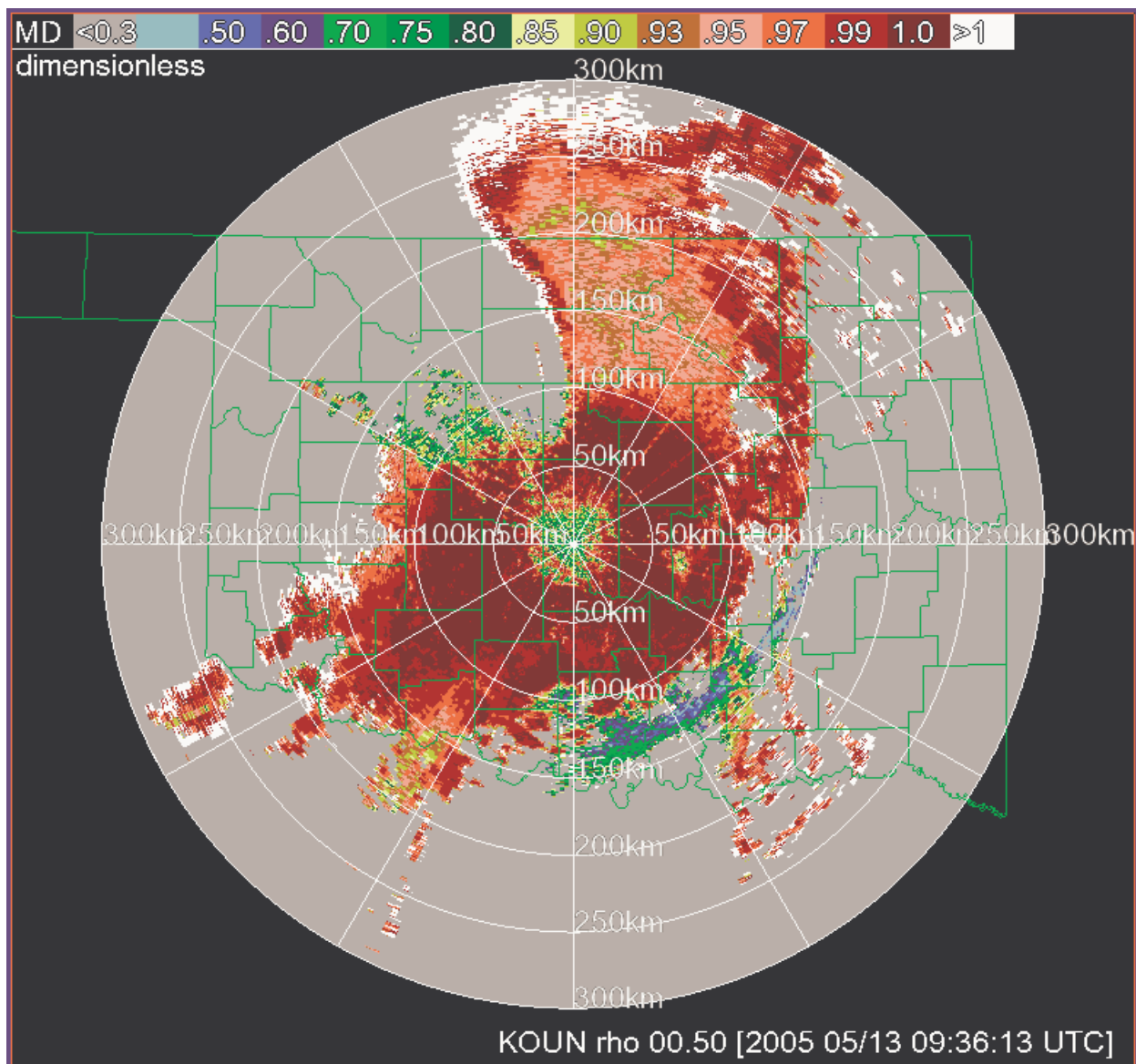*a. Upgrades to the Hydrometeor Classification Algorithm*

Figure 3. PPI of cross-correlation coefficient.

The HCA exploits properties of the polarimetric measurements to discriminate between various hydrometeor types and identify non-meteorological targets using a fuzzy logic scheme. Essentially, the algorithm computes a numerical score that represents the likelihood of a particular hydrometeor type based on membership functions of nine interest fields that represent the polarimetric variables and temperature. The scores are weighed and summed for hydrometeor type, and the type with the highest weighted sum is assigned at individual radar bins. The algorithm is most sensitive to radar reflectivity (Z_H), differential reflectivity (Z_{DR}), and temperature.

Early versions of the HCA often designated rain layers above the freezing level when the input temperature profile taken from either unrepresentative atmo-
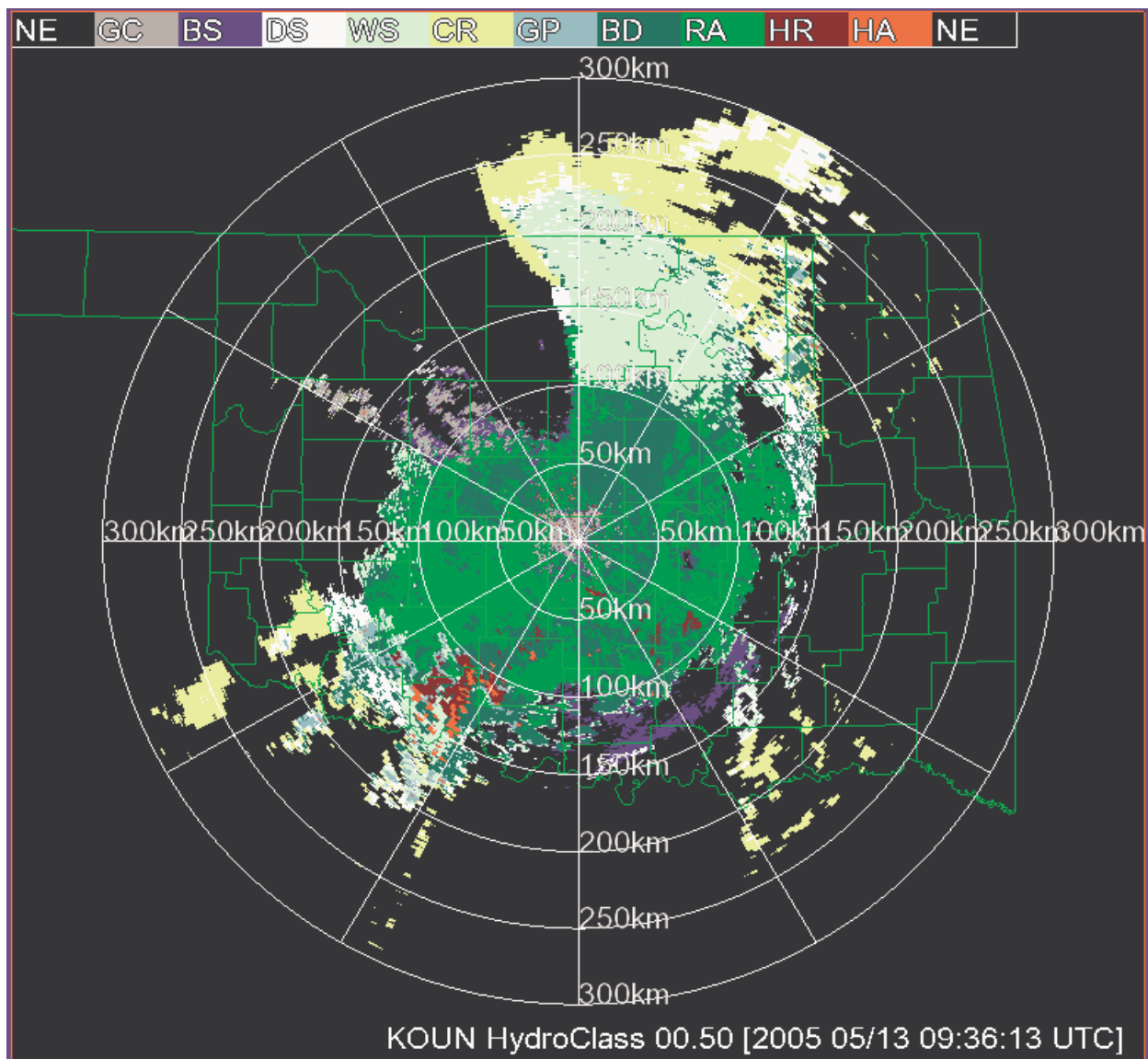
Figure 4. Results of classification produced by the new scheme. GC - ground clutter / AP; BS - biological scatterers; DS - dry aggregated snow; WS - wet snow; CR - crystals; BD - "big drops", RA - light and moderate rain; HR - heavy rain; HA - hail.

spheric soundings or numerical forecast models had a freezing level height that was too high. This temperature bias has been corrected by using the polarimetric Freezing Level Algorithm described by Brandes and Ikeda (2004). The FLA determines the 0°C height by examining pronounced melting signatures in the Z_H, linear depolarization ratio (L_{DR}), and correlation coefficient (ρ_{HV}) measurements (e.g., Fig. 6). The estimated freezing level height, shown as a horizontal line, is 2.64 km MSL. Once the temperature bias is found at the radar-based freezing level height, the temperature profile is adjusted accordingly.

A simple consistency check now eliminates other spurious rain designations that arise from unusual combinations of polarimetric variables. As an example,
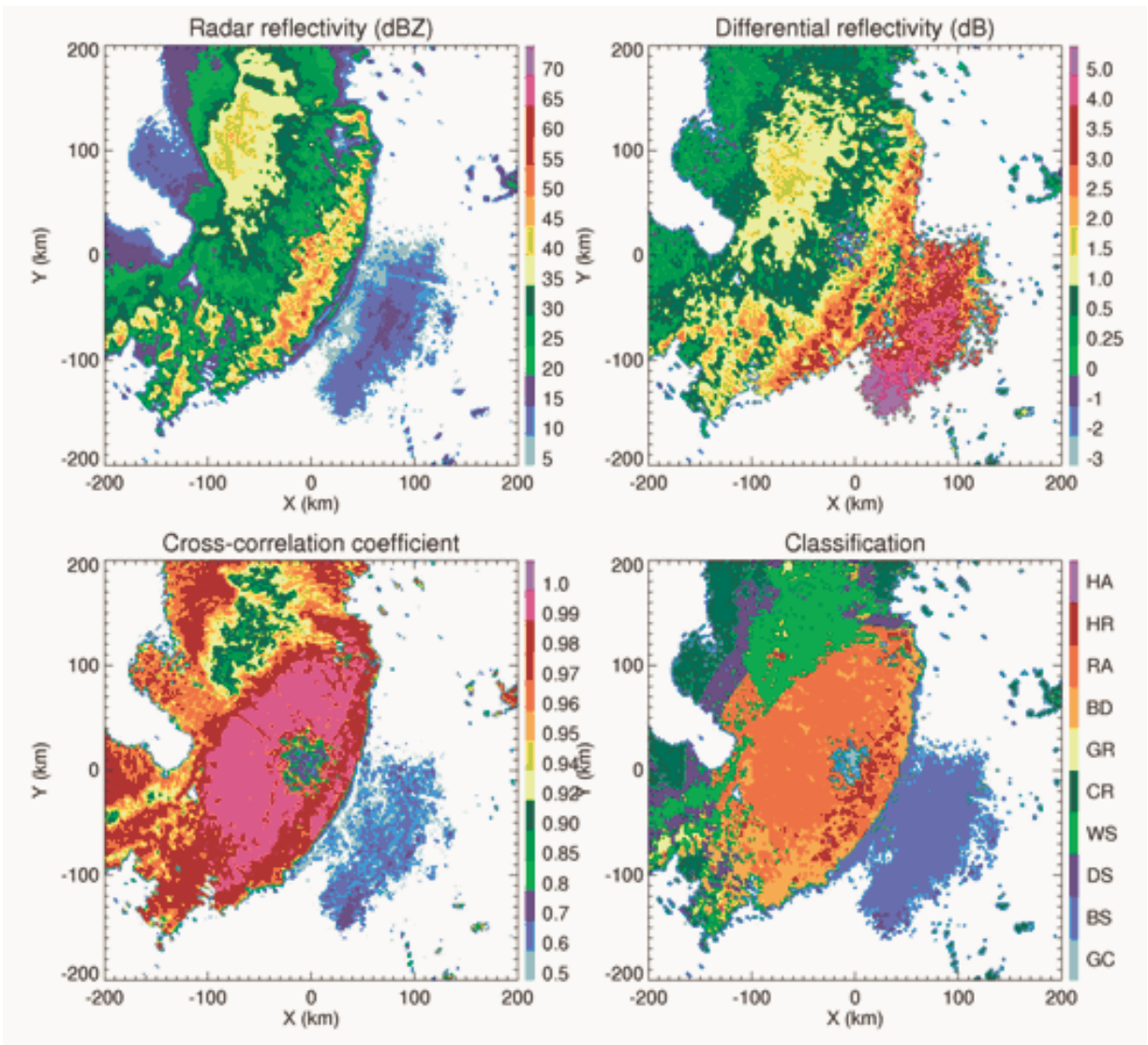
Figure 5. Composite plot of Z, Z_{DR}, ρ_{hv}, and results of classification for the case on May 13, 2005 (0758 UTC), elevation 0.5°

Fig. 7a shows a thin layer of light rain (LR) designations just below the 0oC level (the dash line) and above a layer of wet melting snow (WS) as deduced from the radar measurements (Figs. 7c-f). Inspection of the data points revealed that the light rain designation was based on large Z_H, relatively small Z_{DR}, low L_{DR}, and high ρ_{HV} which produced large weighted sums for both the light rain and dry snow categories but a slightly higher score for light rain. Light rain was designated because the temperature in this layer was >0°C. Most likely the hydrometeors were melting snow. In order to reduce such unphysical designations, the updated HCA performs a consistency check of the assigned particle types in the melting layer and suppresses rain designations in the layer bounded by the freezing level and the melting layer signature maxima. By eliminating the rain category, either dry snow or wet snow is designated (Fig. 6b).
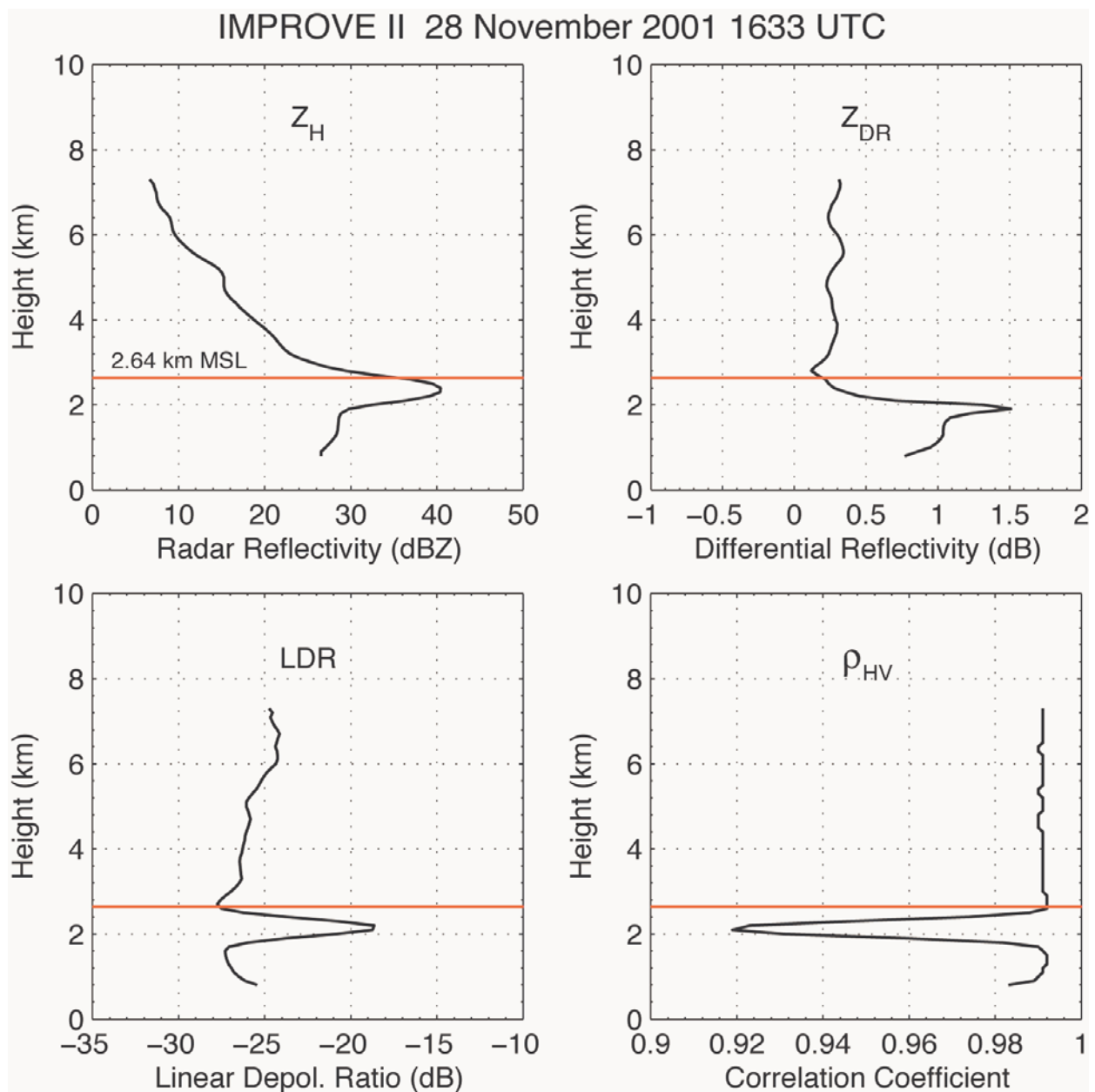
Figure 6. Profiles of polarimetric measurements (ZH, ZDR, LDR, and ρHV) for 1633 UTC on 28 November 2001 during the IMPROVE II. The estimated 0°C level (2.64 km MSL) is shown by a red line.

The consistency check is robust because of the strong signatures of L_{DR} and ρ_{HV} in the melting layer for stratiform rain.

b. Detection of in-flight icing conditions

HCA testing on datasets from the IMPROVE II project disclosed a tendency to over "predict" supercooled liquid drops in the upper levels of storms where the temperature was much too cold to support significant concentrations of super-
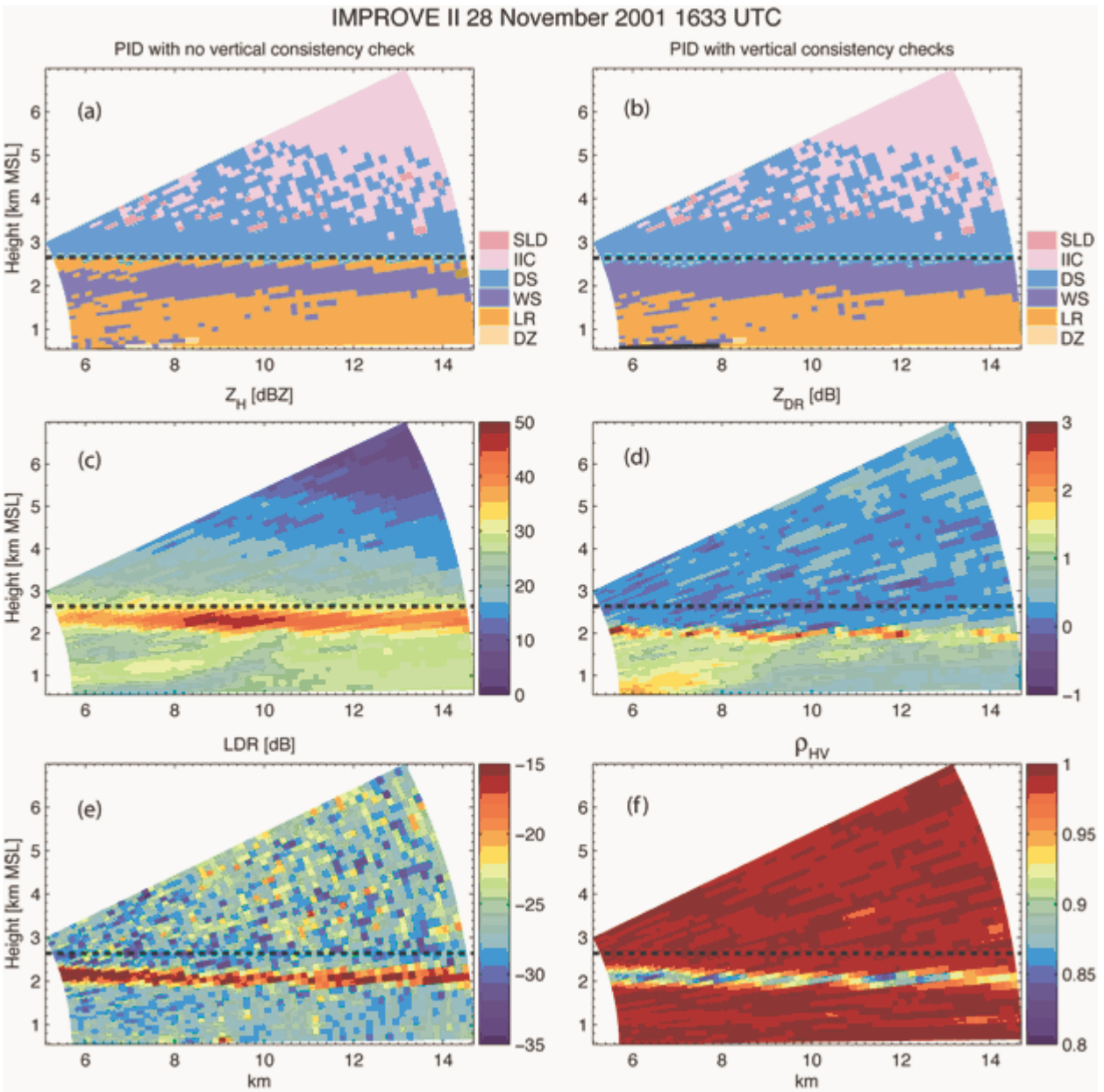
Figure 7. Cross-sections of (a) hydrometeor designations without a consistency check (see text), (b) hydrometeor designations after the consistency check, (c) Z_H, (d) Z_{DR}, (e) L_{DR}, and (f) ρ_{HV} for 1633 UTC through the 95° azimuthal direction. The freezing level height (2.64 km MSL) is indicated by a dashed line. Hydrometeor categories are listed to the right of Figs. 2a-b. SLD: supercooled liquid drops, IIC: irregular ice crystals, DS: dry snow, WS: wet snow, LR: light rain, and DZ: drizzle.

cooled liquid drops. The HCA was modified to use the temperature membership function of the Current Icing Potential algorithm (Bernstein et al. 2005). The new membership function is based on observations from past field programs and a climatological study of the pilot reports (PIREPs) of in-flight icing. The membership function assigns the maximum chance of supercooled liquid

drops to temperatures between -8 and -4°C and decreases the probability of icing to zero at -26 and 0°C. The new membership function significantly reduces supercooled liquid drop designations at the tops of cold precipitation layers without affecting the other parts of the cloud. Icing designations at cloud tops should be further improved by incorporating experimental satellite products being developed by NASA.

Another area of active research has been the examination of polarimetric signatures in icing conditions using data collected during past field programs. Precipitation-sized supercooled liquid drops can be particularly hazardous to aircraft due to the impaction and freezing of the drops beyond deicing boots, leading to a significant reduction in aircraft performance. During the IMPROVE II field campaign, the NOAA P-3 and the University of Washington Convair experienced icing conditions on 14 December 2001. Figure 8. shows vertical
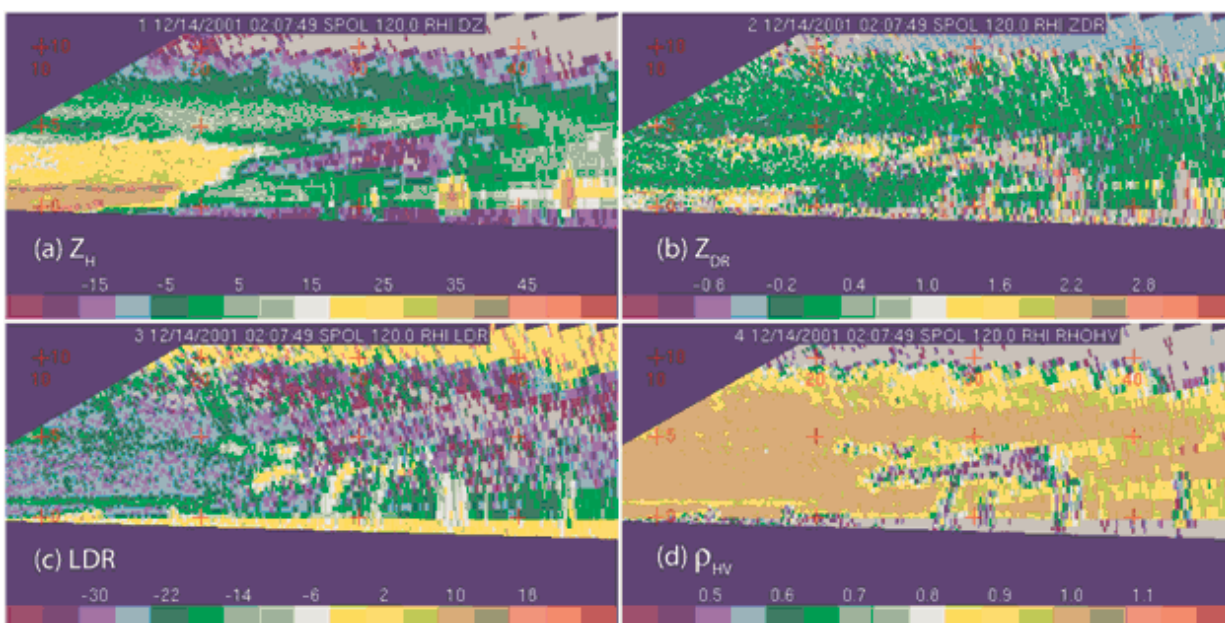

Figure 8. Cross-sections of (a) Z_H, (b) Z_{DR}, (c) L_{DR}, and (d) ρ_{HV} at 0208 UTC on 14 December 2001 for an azimuth angle of 120°. The ordinate is height above the ground level in km. Tick marks (in red) are 5 km in the vertical and 10 km in the horizontal.

cross-sections of radar variables through an icing region. An altostratus cloud layer at 6 km AGL existed above weak low-level orographic precipitation. The 0°C level was at 2.0 km MSL (~1.5 km AGL). The NOAA P-3 reported icing associated with supercooled drizzle while flying through the weak echo region at 2.6 km MSL and a radar range of 24 km, near the top of the lower orographic cloud layer (see Fig. 9 for location). The temperature at flight level was -3°C.

Figure 9 shows hydrometeor designations from the HCA associated with the measurements in Fig 8. Irregular ice crystals are designated throughout most of the elevated altostratus layer as observed by the Convair. Designations of
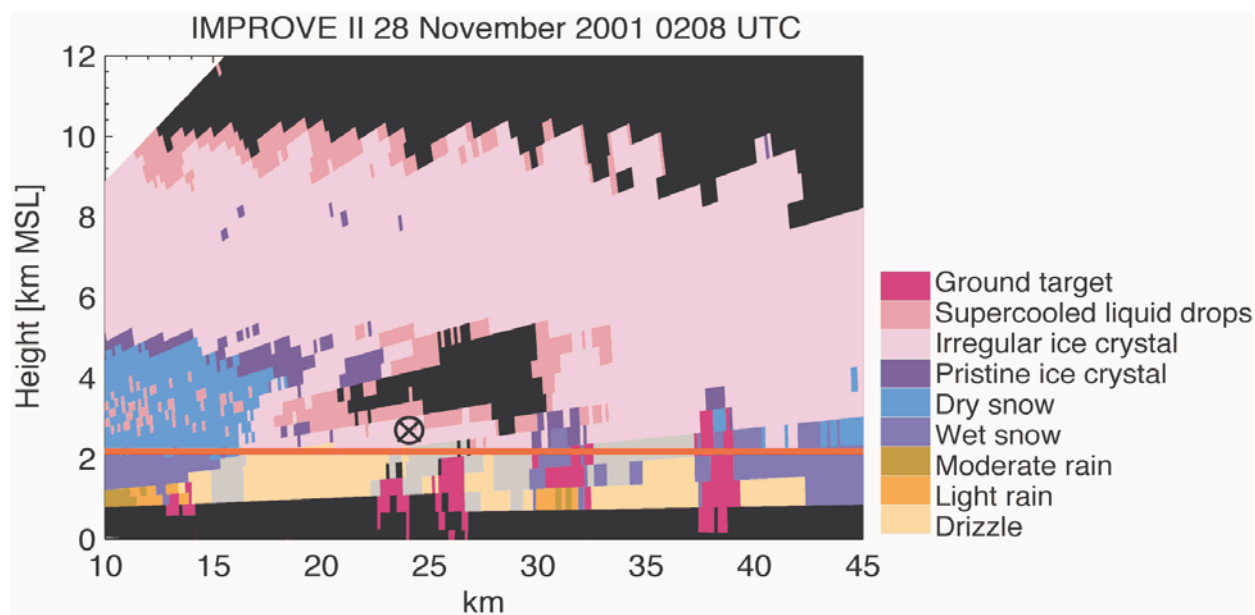
Figure 9. Hydrometeor designations for a portion of the cross-section in Fig. 7. Hydrometeor categories are listed on the right. The crossed-circle indicates the location of the P-3 aircraft (coming out of the figure plane). The radar data were advected in time to match the aircraft location.

supercooled liquid drops are made at the top of the shallow lower orographic cloud layer near the P-3 location (20-33 km). However, surface observations suggest that the supercooled liquid drop layer actually extended to ground because freezing drizzle was observed at ground. The problem is under investigation but is compounded by the presence of strong ground targets and relatively weak radar signals. We are currently examining the relationships among the polarimetric variables, such as the correlation between Z_H and Z_{DR} and texture parameters in an attempt to retrieve more information from the radar measurements. This investigation is also being expanded to include icing and non-icing conditions from the MAP field program.

References

Bernstein, B. C., F. McDonough, M. K. Politovich, B. G. Brown, T. P. Ratvasky, D. R. Miller, C. A. Wolff, and G. Cunning, 2005: Current icing potential: Algorithm description and comparison with aircraft observations. *J. Appl. Meteor.,* **44,** 969–986.

Brandes, E. A., and K. Ikeda, 2004: Freezing-level estimation with polarimetric radar. *J. Appl. Meteor.,* **43,** 1541?1553.

b) Planned Efforts

Continue with scheduled work plan.

c) Problems/Issues

None.

d) Interface with other Organizations

None.

e) Activity Schedule Changes

None.

06.6.25 Polarimetric Freezing Level Detection.

An ability to detect the freezing level within clouds and precipitation is important for establishing in-flight icing hazards and for winter-weather products such as rain-snow discrimination. Designated freezing levels may also prove useful for more accurate numerical model initialization and thereby improve forecasts of hazardous weather. A fast-track non-polarimetric version of the freezing-level detection algorithm could be implemented in just a few years which may improve products like the Current Icing Potential (CIP) algorithm without having to wait for dual-polarization upgrade to the WSR-88D.

a) Current Efforts

See 06.6.22.

b) Planned Efforts

Continue with scheduled work plan.

c) Problems/Issues

None.

d) Interface with other Organizations

None.

e) Activity Schedule Changes

None.

05.6.26 Polarimetric winter quantitative precipitation estimation.

Winter quantitative precipitation estimation (QPE) is important to winter weather algo-rithms and ground de-icing operations. Current systems adjust radar-based winter QPE using measurements from in situ sensors such as gauges. A capability to retrieve particle size distributions and to discriminate among various hydrometeor types with polarimetric radar should lead to better predictions of winter storm precipitation inten-sity and, consequently, to more efficient ground de-icing activities, enhanced flight safety, and increased airport capacity.

a) Current Efforts

A manuscript that summarizes some characteristics of winter storms as deter-mined by video disdrometer observations (attached as Appendix 2) was sub-mitted to the Journal of Applied Meteorology and Climatology. This study was conducted to improve the discrimination of frozen hydrometeor types and quan-tification of winter precipitation with polarimetric radar. The study also has implications for the parameterization of microphysical processes in winter storms. Efforts have shifted to the study of the interrelationships between envi-ronmental meteorological factors and particle distributions in winter storms. Currently, disdrometer data from storms in which precipitation changes from rain to snow are being examined to determine the likelihood that precipitation is snow, given the temperature and relative humidity. The information will be ingested by the HCA to improve the discrimination between rain and snow. The information is of interest to the Winter Weather PDT for rain?snow discrimina-tion with the Weather Support to Deicing Decision Making (WSDDM) system and is needed for estimating precipitation-impacted visibility and to improve quantitative estimates of winter storm precipitation.

The sensitivity of radar reflectivity and differential reflectivity calculations with video disdrometer measurements to assumed snow particle axis ratios was examined using data collected on 5 March 2004 during the WISP04 field exper-iment. Using the disdrometer observations, axis ratio-hydrometeor size rela-tions were developed for storm stages dominated by aggregates and graupel. The derived relations and a previously derived density–size relation were then used to compute backscattering amplitudes of snow via the Rayleigh-Gans approximation method. Z_{DR} was calculated for the observed snow particles and compared to the radar measurements. The results showed that the dis-drometer-derived axis ratio–size relationships damp out the temporal variation of Z_{DR}. The reason for the less-variant Z_{DR} when using the axis ratio–size rela-tionships is attributed to a less oblate appearance of snow particles on the aver-age with the disdrometer, which is perhaps related to instrument-induced turbulence. The best correspondence between the radar and the disdrometer was achieved when using a fixed axis ratio of 0.7 or 0.8.

b) Planned Efforts

Continue with scheduled work plan.

c) Problems/Issues

None.

d) Interface with other Organizations

None.

e) Activity Schedule Changes

None.

06.6.29 **NCAR NTDA Implementation in NEXRAD OpenRPG/CODE. (NCAR).**
Collaboration with the Turbulence PDT for the WSR-88D ORPG implementation of the NCAR Turbulence Detection Algorithm (NTDA) is a task that allows AWRT to collaborate with this PDT in their goal of having a national, 3-D turbulence product for aviation users. The Turbulence PDT has developed the turbulence algorithm. The AWRT PDT will collaborate with the Turbulence PDT in the implementation of NTDA within the WSR-88D environment. This assistance includes hardware purchases, software acquisition of the ORPG CODE and software engineering assistance.

a) Current Efforts

Continuing the effort begun in FY05, implement the NCAR Turbulence Detection Algorithm in the NEXRAD OpenRPG Common Operations and Development Environment. Complete software coding and unit system testing to ensure consistency with the prototype algorithm. Modify the algrotihm as appropriate to handle idiosyncrasies in the OpenRPG environment, take advantage of other available OpenRPG products, and minimize use of system resources based on the results of benchmarking tests. In conjunction with Thrubulence PDT verify that any required algorithm modifications do not degrade performance. Complete all algorithm descriptions, specifications, and documentation required by the FAA or NEXRAD TAC and SREC approval processes. Support attendance by project staff at TAC and SREC meetings as necessary to obtain implementaion approval.

With guidance from Betty Bennett and Dave Smalley of MIT Lincoln Laboratories, the RAL installation of OpenRPG/CODE has been set up to run on real-time LDM data.

After initial benchmark tests suggested that the initial ORPG/CODE implementation of the NTDA required significantly more system resources than other ORPG algorithms, code profiling and optimization are being performed. These have already yielded significant reductions in system resource requirements.

A briefing on the NTDA was presented at the NEXRAD Technical Advisory Committee's March 21-22 meeting. Although formal feedback has not yet been received, a member of the committee reported that the TAC found the NTDA science adequate for operations, but that a more specific statement of requirements and sponsorship from the FAA was needed.

The NTDA Casefile was formally submitted and a Configuration Change Request number assigned. It is CCR #NA06-09601, "IMPLEMENTATION OF THE NEXRAD TURBULENCE DETECTION ALGORITHM (NTDA) IN THE NEXRAD OPEN RPG".

Numerous contacts at MIT/LL, the FAA and the ROC have provided information, templates, sample documents and advice on getting a new NEXRAD ORPG algorithm accepted and deployed.

b) Planned Efforts

Working with the Turbulence PDT task 06.7.3.1.1, continue to enhance the NTDA, tune its parameters, implement code optimization and pursue algorithm simplification as needed to reduce resource requirements to an acceptable level.

Continue to run the NTDA on real-time LDM data to verify the CODE implementation's stability.

Perform an NTDA code review with senior software engineers at NCAR/RAL.

Continue pursuing the NTDA approval process. In particular, an NTDA Design Approach Review with ROC software engineers will be scheduled, and a briefing on the NTDA to the NEXRAD Software Recommendation and Evaluation Committee is scheduled for May 2.

c) Problems/Issues

A specific FAA requirement for the NTDA and statement of sponsorship may be a prerequisite to its acceptance for integration into the WSR-88D baseline.

Uncertainty about whether the Turbulence PDT's GTG-Nowcast product will run at NCEP/AWC or NCEP/CCS may complicate definition of the NTDA concept of operations and delay its deployment.

d) Interface with other Organizations

NWS Office of Science and Technology and Radar Operations Center, BAE Systems, NEXRAD TAC, NEXRAD SREC

e) Scheduled Activity Changes

None.

06.6.34   High-Resolution National 3-D Radar Mosaic

The area for which any arbitrary ARTCC or AFSS has responsibility encompass the coverage area of several WSR-88D installations. Numerical models have reached such a level of sophistication that they now use radar data to initialize model runs. There are no existing products that use data from more than one radar, and no gridded products that use the full 3D characteristics of these data. The real-time CONUS 3D mosaic system will be stabilized and enhanced in FY 2005 based on the findings during FY 2004. The AWRT can also provide customized products as requested by other AWRP PDTs. For example, a suite of 2-D products will include VIL (vertically integrated liquid), hail products, and layer composite reflectivities will be derived from the 3D mosaic. This task supports several other PDTs by providing them with full 3D grids and derived 2D grids that take advantage of 3D and 4D information.

a) Current Efforts

06.6.34.1 Continued evaluations and enhancements of the reflectivity QC procedure

Activities during this quarter included the continued identification and archiving of case examples for QC assessment and diagnosis. The cases are identified (often in real-time as the events transpire) using the NSSL National Mosaic and QPE (NMQ) system, in which the national 3-D mosaic is a major component. The QC techniques used in the National 3-D Mosaic application are continually assessed and enhanced. During the past quarter a neural net approach developed by Lakshmanan et al. (2006) was examined towards improving radar QC within the real time national 3D mosaic grid products. Figures 1 and 2 depict results from two cases initially examined. The figures depict a performance comparison of single radar reflectivity with A) no QC adjustment, B) the QC adjustment using a neural net (QCNN), and C) a heuristic QC scheme used in the NMQ system that combines noise filters, physical rules, and REC components.

The first case, shown in Fig. 10, highlights one of the more challenging QC situations where storm cells are encompassed within a larger region of AP (anomalous propagation). While both the QCNN and the heuristic technique remove a significant portion of the AP, the QCNN removed real echo at farther ranges (see red circles in Fig. 10). The heuristic QC removed slightly less of the AP in comparison to the QCNN but did not remove the storm cell at long range. However, the heuristic QC did leave residual AP artifacts (denoted by orange circle in Fig. 10C) as a result of a rule-based vertical reflectivity gradient check that was range and azimuth dependant. The second case, shown in Fig. 11, consists of a large AP area in addition to higher intensity clutter near the radar and adjacent to the radar as result of the large buildings in downtown Chicago (see red circles in Fig. 11). While both techniques removed all of the AP, the QCNN left the ground clutter targets resulting in a field of reflectivity 'speckles.' The
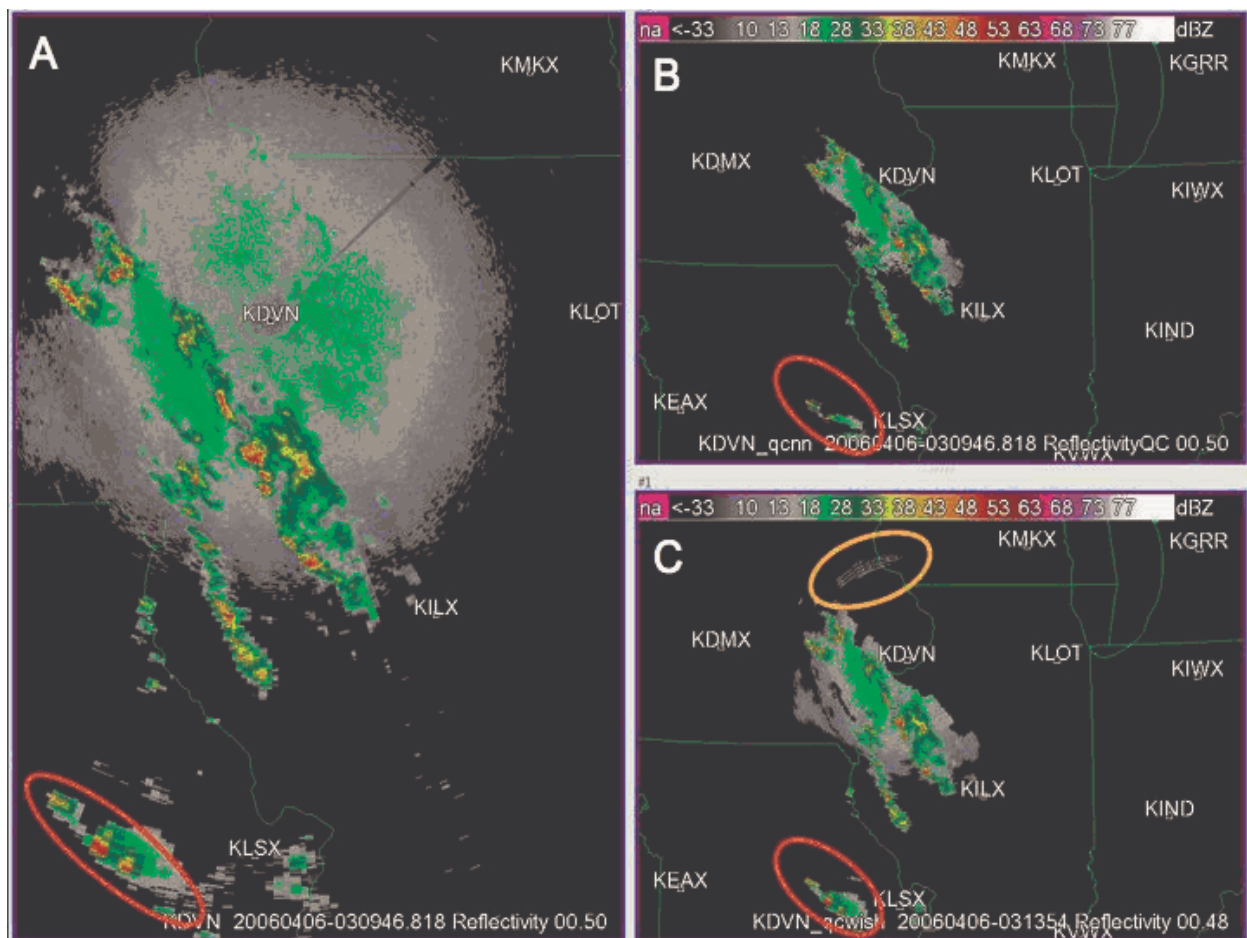
Figure 10. Example base reflectivity fields at the lowest tilt (0.5 degree) from raw observations of KDVN radar (A) and after quality control process using the QCNN technique (B) and the heuristic QC technique (C). The data are valid at 03:09:46UTC on 6 April 2006.

heuristic technique effectively removed all non-precipitation echoes for this case.

Other cases initially examined yielded similar results. While both the QCNN and heuristic QC techniques performed equally in removing the AP, the heuristic methodology left residual artifacts of varying magnitude. The QCNN, while it removed real echoes at far ranges and was ineffectual at removing clutter, can be trained to address the issues of AP associated with cityscapes and other features such as terrain features and coastlines. Further, the QC assessment case archive can serve as the basis for training the QCNN application. The future work will involve continued analysis and comparisons of QC methodologies towards a real time QC implementation that will encompasses components of both the heuristic and neural network QC. Additionally, a satellite-based effective cloud cover mask will be implemented as the last step to remove residual clear air/insects, AP, and other non-precipitation/non-clouds radar echoes (such as chaff) in the national 3D mosaic product grids.
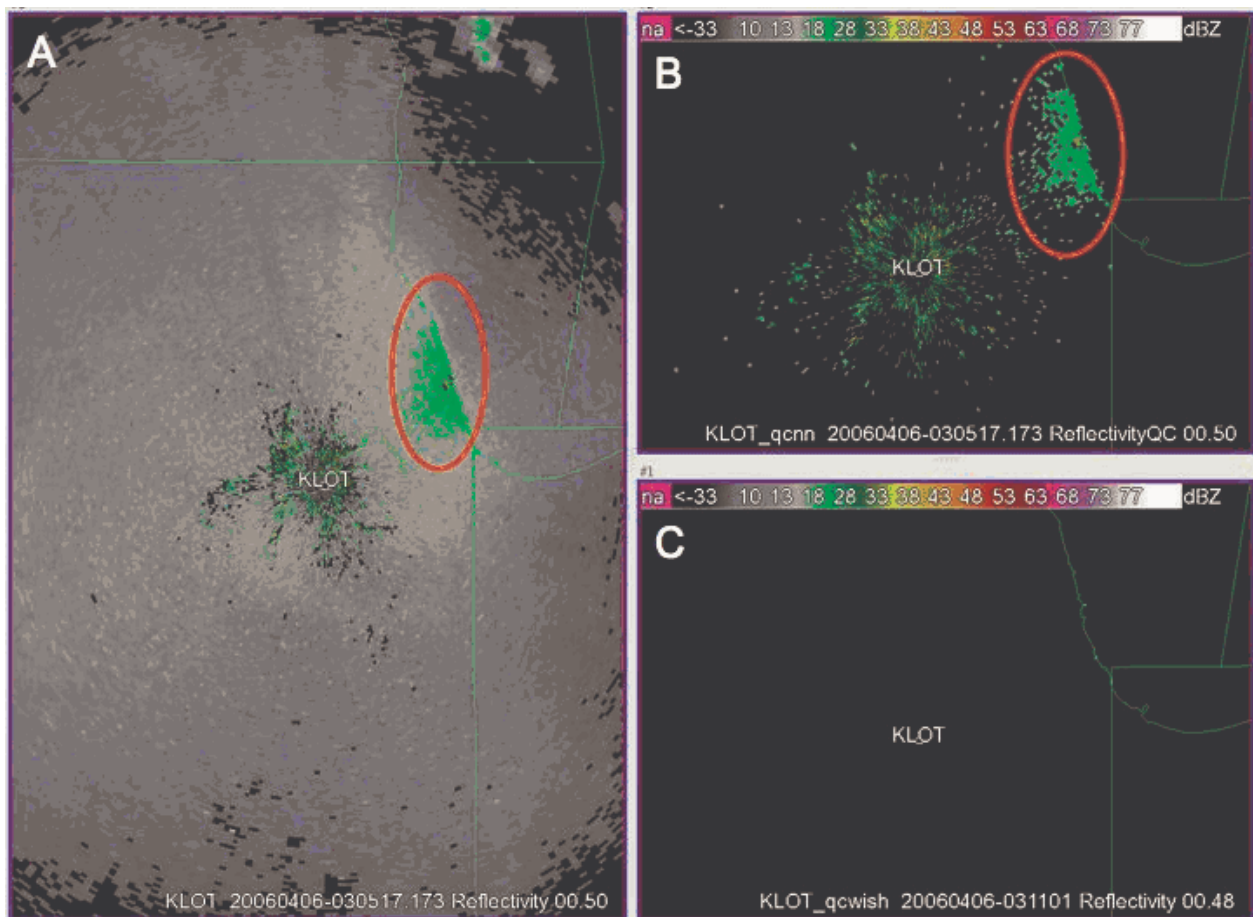
Figure 11. Example base reflectivity fields at the lowest tilt (0.5 degree) from raw observations of KLOT radar (A) and after quality control process using the QCNN technique (B) and the heuristic QC technique (C). The data are valid at 03:05:17UTC on 6 April 2006.

06.6.34.2 Continued development of a gap-filling scheme using vertical profiles of reflectivity.

Activities during this quarter included the continued development and testing of the VPR (vertical profile of reflectivity) based gap-filling scheme. The gap-filling scheme segregates precipitation echoes in a radar umbrella area into two types: convective and non-convective. The scheme assumes that all the convective precipitation echoes have the same vertical structure but with varying magnitudes, as does the non-convective precipitation echoes. The vertical structures of the two types of precipitation 'classes' are described by two vertical profiles of reflectivity, or VPRs, derived from the volume scan of base level reflectivity data within a pre-specified annular region (Fig. 12a). The annular region was chosen as a balance between: 1) the need to be away from the radar origin to minimize the impact of potential ground clutter, and 2) the need to be close to the radar so that the beam spreading is not very large and high vertical resolution can be represented in the VPRs. The VPRs are computed from each volume scan, and therefore are dynamically evolving with time. A
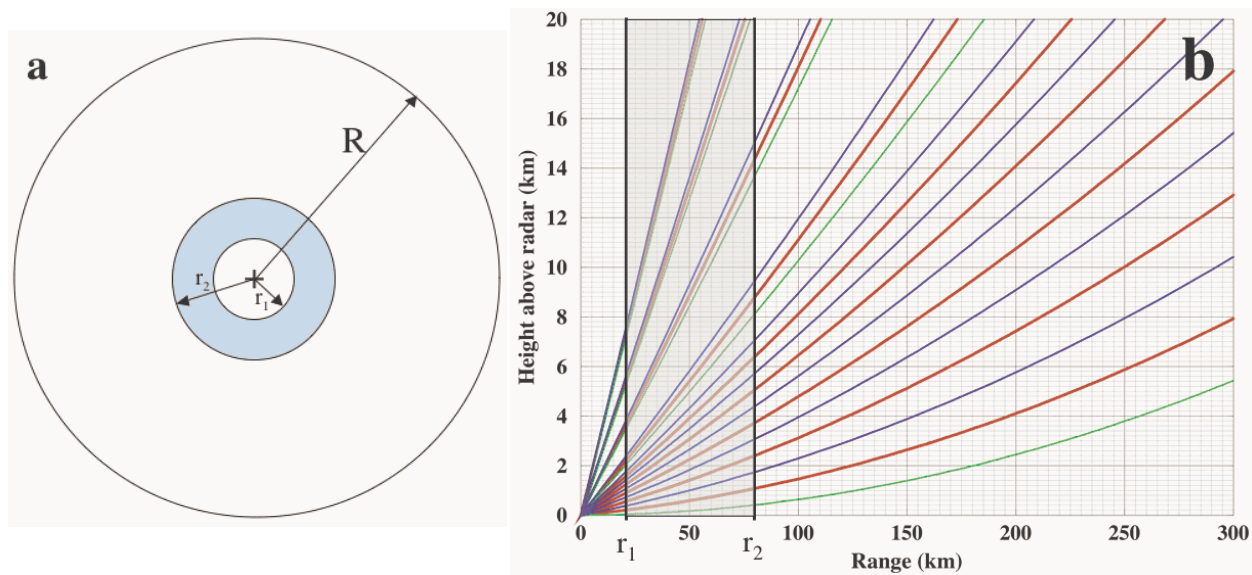
Figure 12. A top view (a) and a side view (b) of the annular region (cyan color shaded area) for VPR computation. Here R represents the size of the radar umbrella; r1 and r2 represent the inner and outer bounds of the VPR annular region.

running hourly average is applied to the single volume scan VPRs to obtain hourly mean convective and non-convective VPRs, which are less prone to random errors. The hourly mean VPRs are then used to extrapolate radar observations from the lowest tilt down to the elevation of the radar.

During this quarter, the gap-filling scheme was tested using the hurricane Isabel case analysis. The VPRs used for the gap-filling were obtained from the case study reported in the last quarter (see the 1st quarterly report of AWRT for task 06.6.34.2). The results of the gap filling are presented under task 06.6.34.3 in current quarterly report.

06.6.34.3 Develop evaluation methods for the gap-filling technique using vertical profiles of reflectivity.

Activities during this quarter included the continued evaluation of the VPR-based gap-filling scheme using single radar Cartesian (SRC) grids. Volume scans of base level data from several radars in the North Carolinas were first remapped onto 3-D SRC grids. The SRC grids are centered on each radar site with a horizontal resolution of 0.01° × 0.01° (in a cylindrical equidistant map projection). The SRC grid derived for each radar has the same 31 vertical grid levels with the lowest level at 500 m extending to 18km above mean sea level (Fig. 13). The remapping scheme from the radar native spherical coordinates to the Cartesian grid follows the vertical interpolation scheme of Zhang et al. 2005.
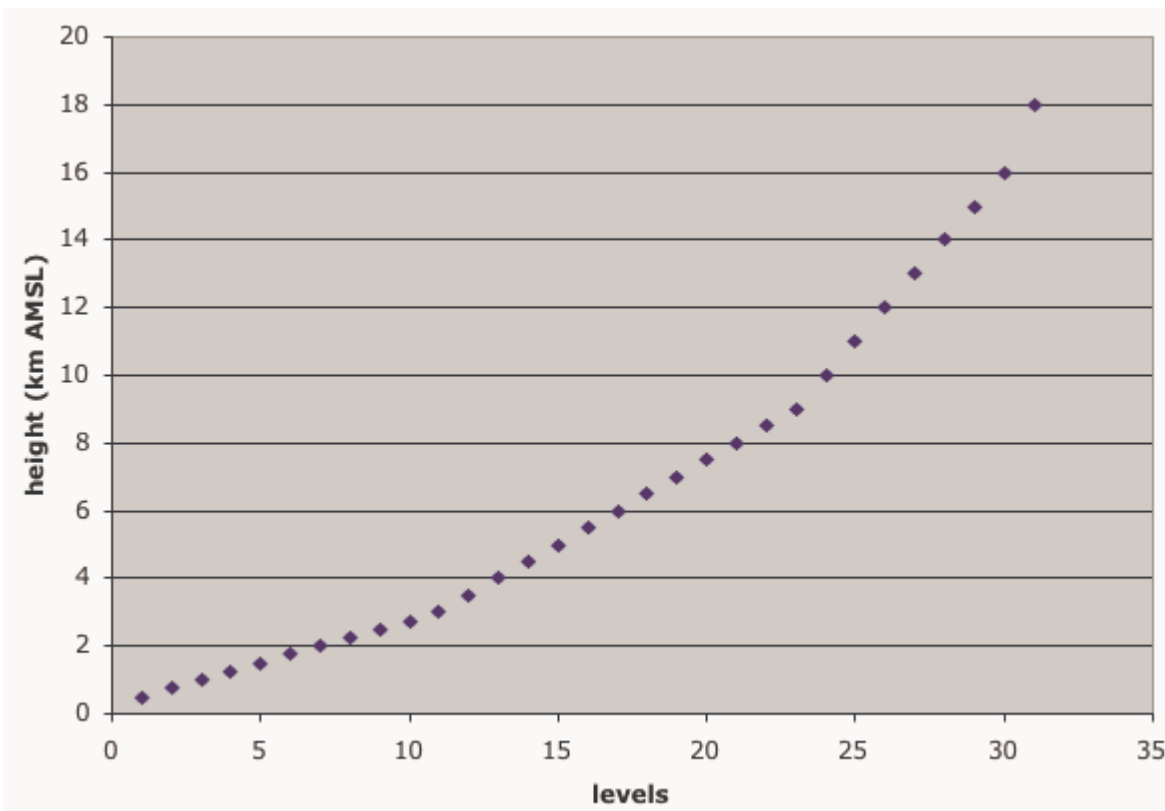
Figure 13. Height distributions of the vertical levels in the single radar Cartesian grid.

Figure 14 shows horizontal cross sections of the SRC grid reflectivities from 3 radars located in North Carolina and Virginia during the hurricane Isabel event. The circular echo boundaries correspond to where the 1-km height level intersects the bottom of the lowest tilts. The radar coverage at lower levels (Fig. 5) is limited due to the earth curvature and position elevation angles used in the WSR-88D scan strategies.

The gap-filled SRC grids from KMHX radar are compared with the original SRC grid from the nearby KRAX radar. Figure 15 shows horizontal cross sections of gap-filled SRC grid (Fig. 15a) and of the SRC grid without gap filling for KMHX radar (Fig. 15b). The gap-filling scheme significantly improved the depiction of the hurricane at the 1-km (AMSL) height. The overall pattern and intensity of the gap-filled precipitation echoes (Fig. 15a) agrees with the independently observed reflectivity from another radar (KRAX, Fig. 15c). The rain bands to the southwest and to the east of the KRAX radar (Fig. 15c) were effectively captured in the gap-filled field (Fig. 15a).

Figure 16 shows vertical cross sections along a rain band to the southwest of KRAX radar. The rain band was not observed by KMHX at the 1km height level (Fig. 16d). After gap filling, the rain band was successfully recovered (Fig. 16e). The vertical structure of the gap-filled reflectivity field (Fig. 16b) compares very
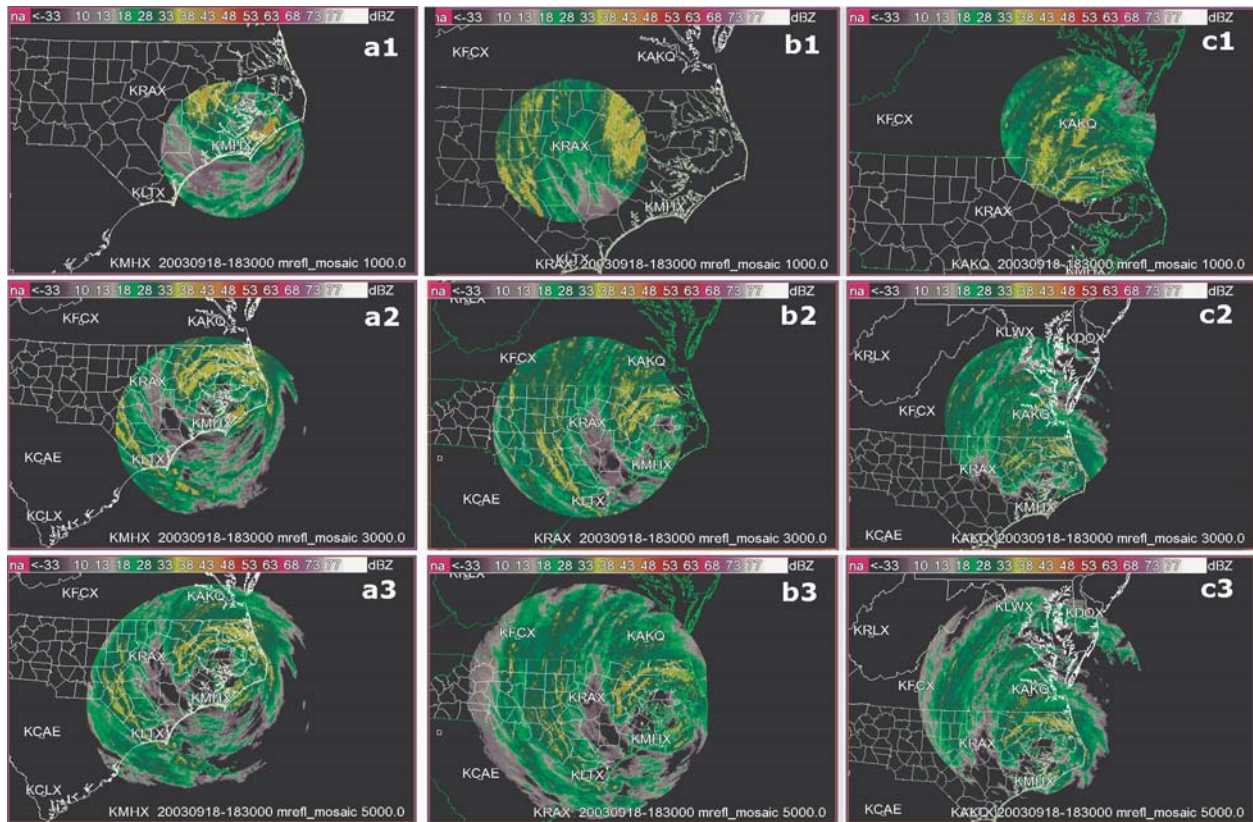
Figure 14. Horizontal cross sections of the SRC grid reflectivity fields on 1km (row 1), 3km (row 2), and 5km (row 3) above mean sea level from KMHX (column a), KRAX (column b), and KAKQ (column c) radars.

well with the observed field at the southern end of the cross-section, where it is closer to KMHX radar (Figs. 16b and 16c). However, when the distance is too far from the radar, the vertical structure was not fully recovered (see red circles in Figs. 16a-16c). Within these regions, additional observations from gap-filling radars may be needed to fully capture the precipitation structure if a proximity WSR-88D radar is not available.

Discussions with the NCAR icing PDT on the possibility of creating an un-QC'd national 3D mosaics for supporting aviation icing products development.

06.6.34.4 Continued evaluation and improvement of the multi-radar synchronization technique.

Activities in this quarter include a study on the synchronism of the radars. During the 4th quarter of FY 05, a multi-radar synchronization study was conducted using a squall line event that occurred on 1 June 2005 in central Texas. Reflectivity fields from three 'testing' radars (KFWS, KEWX, KSJT) were advected to the observational times of a validation radar (KDYX). The advection was a linear extrapolation in space and time using vector fields derived by a multi-scale
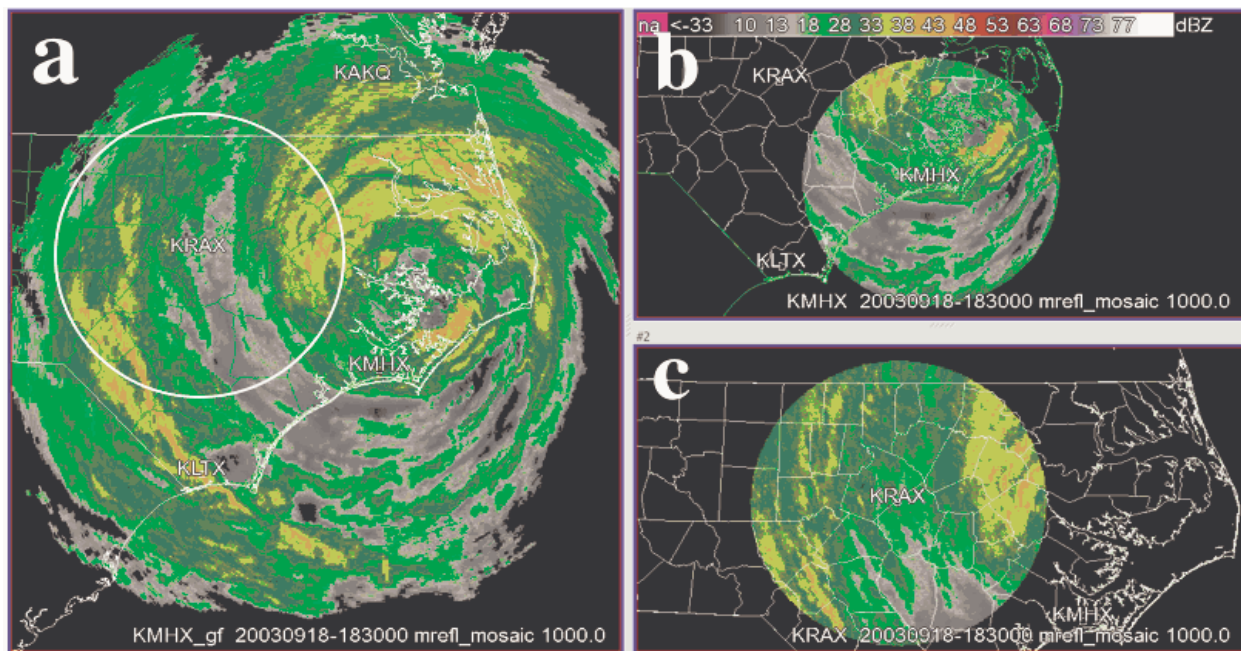
Figure 15. Horizontal cross sections of the gap-filled SRC grid of reflectivity from KMHX radar on 1km (a) and the same cross sections from original SRC grids of KMHX (b) and KRAX (c). The area in the white circle in panel a is corresponding to the KRAX coverage in panel c.

storm clustering and tracking method (see the 4th quarterly report of AWRT for task 05.6.34.4). The advected reflectivity fields from the testing radars were compared with the observations field from the validation radar that was valid at the same time. It was found that the correlation between the advected fields from KSJT radar and the observation from KDYX radar are consistently worse than correlations between the other two testing radars (KFWS and KEWX) and KDYX (Yang et al., 2006). It was suspected that the clock on the KSJT radar was not synchronous in comparison with other radars. This motivated a study of comparing observations (not the extrapolated fields) between the testing radars and the validation radar to evaluate clock synchronism among the radars.

Table 1 shows correlation coefficients between composite reflectivity fields observed by three testing radars (KEWX, KFWS, and KSJT) and by the validation radar (KDYX) on 1 June 2005. The highest correlations (labeled as green in Table 1) between KDYX and KEWX and between KDYX and KFWS mostly occur when their observational times are closest. However, the highest correlations between KDYX and KSJT mostly occur at the times when the KSJT is a few minutes behind KDYX. Since no temporal extrapolation is involved in the fields under evaluation, the time difference between the best correlated KDYX and KSJT volume scans should be due to the clock errors in one of the two radars. In this case, the clock on KSJT radar is probably in error (i.e., a few minutes faster) since the other three radars clocks seem to match well. The clock
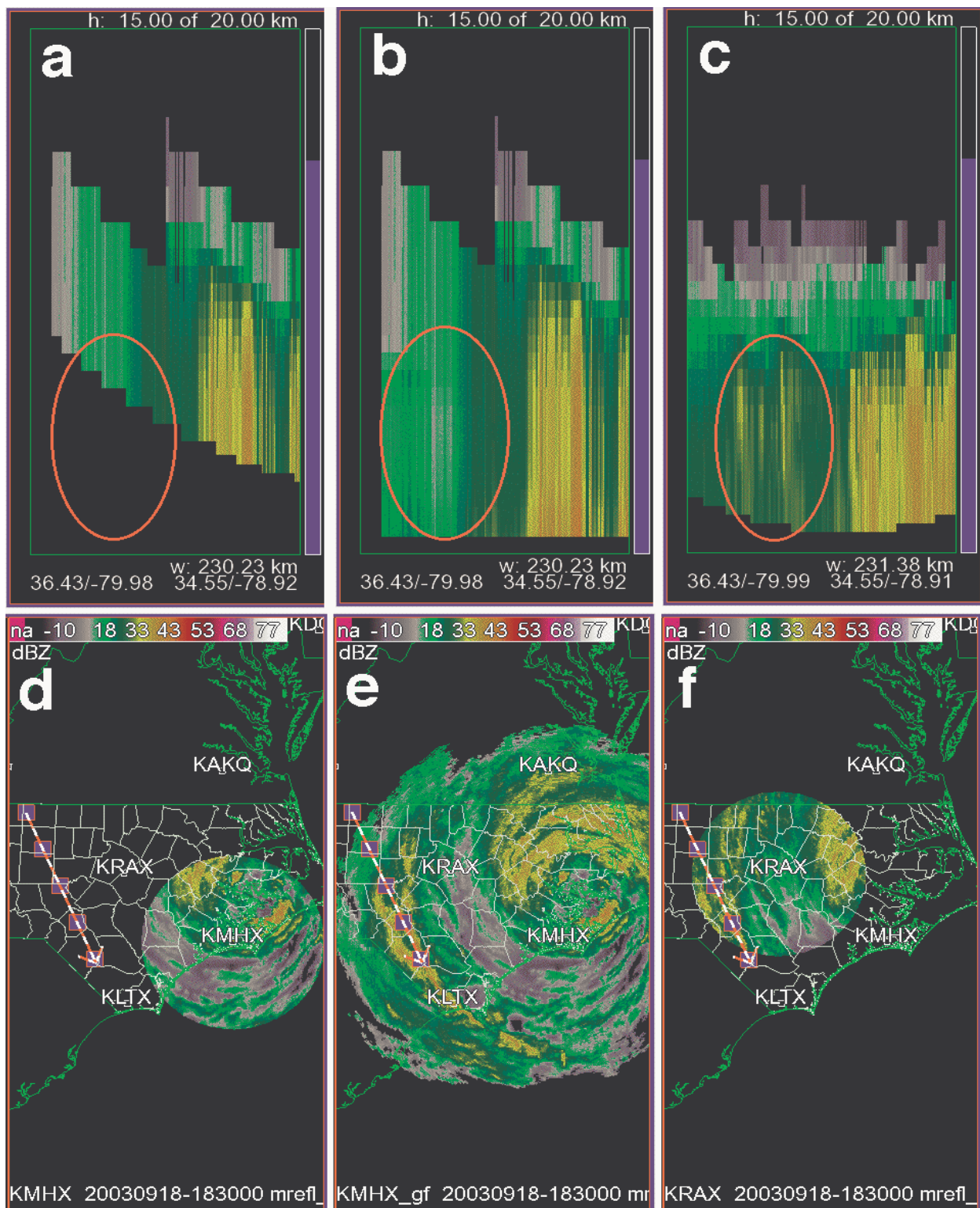
Figure 16. Vertical cross sections of reflectivity fields from SRC grids of KMHX (a) and KRAX (c), and from the gap-filled SRC grid of KMHX (b). The corresponding 1km height horizontal cross sections are shown in panels d, e, and f, respectively. The arrowed lines in the lower panels indicate where the vertical cross sections in upper panels were taken. The red circles indicate regions where the gap-filling scheme did not fully recover the precipitation structure.

error may no longer be an issue once the Open RDAs are installed since the new radar time will be GPS synchronized.

06.6.34.5 Collect Canadian radar data and develop strategies for integration of Canadian radar data into the national 3D mosaic.

During this quarter Canadian base level radar was being received by NSSL. The SRC polar ingest code are being modified to accommodate the Canadian radar non-level 2 format. However, the inter-comparison study between the Canadian and the WSR-88D radar observations will begin in the 3rd quarter due to an infrastructure update in the national 3-D mosaic system (see report on tasks 06.6.35.1 and 06.6.35.2 in the current quarter).

06.6.34.6 Creation and maintenance of user-defined archival process for the CONUS 3-D and 2-D severe weather products.

The activities for this quarter include continued support of the 3D CONUS reflectivity mosaic grid and the related 2D products to several other PDTs.

KDYX	KEWX		KFWS		KSJT	
Obs. Time	Obs. Time	Corr. Coef.	Obs. Time	Corr. Coef.	Obs. Time	Corr. Coef.
05:36	05:30	0.451	05:34	0.669	05:26	0.484
	05:36	0.555	05:39	0.659	05:31	0.623
	05:42	0.390	05:44	0.480	05:35	0.631
					05:39	0.478
05:57	05:53	0.470	05:53	0.610	05:48	0.439
	05:59	0.395	05:58	0.638	05:52	0.594
	06:05	0.059	06:03	0.491	05:57	0.542
					06:01	0.362
06:12	06:05	0.354	06:03	0.374	06:05	0.509
	06:11	0.501	06:08	0.513	06:09	0.645
	06:17	0.311	06:16	0.553	06:14	0.503
					06:18	0.278
06:22	06:17	0.444	06:16	0.437	06:14	0.483
	06:22	0.456	06:25	0.581	06:18	0.667
	06:28	0.305	06:30	0.398	06:23	0.596
					06:27	0.423
06:37	06:28	0.313	06:30	0.362	06:27	0.411
	06:34	0.547	06:35	0.536	06:31	0.631
	06:40	0.488	06:40	0.562	06:35	0.711
					06:40	0.540
06:53	06:46	0.446	06:50	0.509	06:44	0.496
	06:51	0.595	06:55	0.520	06:48	0.677
	06:57	0.449	07:00	0.337	06:53	0.642
					06:57	0.452
0708	0703	0.566	07:05	0.511	06:57	0.457
	0709	0.628	07:10	0.564	07:01	0.685
	0715	0.418	07:15	0.441	07:06	0.754
					07:11	0.613

Table 1. Correlation coefficients between observed composite reflectivity fields from KDYX and from other three radars. Note that the time indicates the UTC time on 1 June 2005 (rounded to the nearest minute) at the middle of the volume scans..

b) Planned Efforts

Continued study of quality control, VPR and gap-filling in the 3D mosaic and time synchronization of multiple radar observations.

c) Problems/Issues

The task 06.6.34.5 for developing strategies for integration of Canadian radar data into the national 3D mosaic will commence in quarter three due to additional work done on tasks 06.6.35.1 and 06.6.35.2.

d) Interface with other Organizations

Regenerated and provided 3-D mosaic data sets based on a request from the CAPS (Center for Analysis and Prediction of Storms, University of Oklahoma) model PDT.

Met with the NCAR turbulence PDT and discussed a collaborative effort towards implementing on the NMQ a national 3D mosaic of eddy dissipation rate (EDR) for supporting aviation icing products development.

06.6.35 Adaptive Radar Mosaic System

This task addresses the availability high-resolution reflectivity data that increases the reflectivity data resolution by reducing the range spacing of reflectivity samples from 1 km to 250 m. This task will develop and evaluate techniques for mapping these new data in the most computationally efficient manner so as to minimize and data latency.

a) Current Efforts

06.6.35.1 Continue optimization of the single radar 3-D Cartesian grids.

(This task has been completed in the first quarter.)

06.6.35.2 Implementation of the single radar 3-D Cartesian grids in the real-time CONUS 3D mosaic.

During this quarter, a new CONUS 3-D mosaic based on the single radar Cartesian (SRC) grid has been implemented. Since the SRC grids have the same horizontal and vertical resolutions and the grid cells are perfectly aligned in overlapping areas, the mosaic is very efficient and flexible. The new mosaic code uses a general scheme that finds all the radars that contributes to a configurable 3-D domain. The domain can be a tile of any size as long as the computational requirements fit in the available hardware. The scheme then combines all the SRC grids using an exponential weighting function described in Zhang et al. (2005).

The new CONUS 3-D Mosaic began running in real-time since 5 April 2006 and will be a part of the NSSL's National Mosaic and multi-sensor QPE (NMQ) system. The new CONUS 3-D Mosaic is replacing the old national 3-D mosaic system that will be taken down on 15 April 2006. Announcement has been sent to all the 3-D Mosaic product users along with the documentation that describes the new product domain and the new product format.

There are currently two types of products generated and available to users. These include:

1.Data files

There are two sets of data files available to the users:

i)3-D reflectivity mosaic grid
ii) 2-D storm products derived from the 3D reflectivity mosaic grid, which include the following 13 data fields:
· composite reflectivity (cref)
· height associated with the composite reflectivity (hgt_cref)
· echo top (etp18)
· severe hail index (shi)

· probability of severe hail (posh)
· maximum estimated hail size (mehs)
· hybrid scan reflectivity (hsr)
· height associated with the hybrid scan reflectivity (hsrh)
· low-level composite reflectivity (lcref)
· height associated with low-level composite reflectivity (hgt_lcref)
· vertically integrated liquid (vil)
· VIL density (vilD)
· precipitation flag (convective/non-convective) (pcp_flag)

2.Images

The users will be provided with access to the NMQ web page (http://nmq.ou.edu/~qpeverif/Main/) where they can view images of the 2-D products both in real-time and retrospectively (up to 6 months or more if the hardware allows). The 2-D image products include the 13 storm products mentioned above. Additionally, the NMQ web page will include but not limited to:

UnQC'd composite reflectivity,
Satellite IR image,
Satellite effective cloud amount,
RUC surface temperature

The new CONUS 3-D Mosaic will be continuously monitored and evaluated. Any issues and subsequent improvements/updates will be reported in quarterly reports.

06.6.35.3 Investigate the adaptation of the new QC techniques developed for the 3D mosaic to polarimetric data fields.

This task is removed from this year due to the 11% funding cut.

06.6.35.4 Investigate and develop strategies for mosaicing polarimetric data fields

(This task starts in the 4th quarter.)

b) Planned Efforts

Continued evaluation and enhancements of the new CONUS 3-D mosaic based on the SRC grids and the adaptive mosaic system.

c) Problems/Issues

The task 06.6.35.3 is removed from this year due to the 11% funding cut.

d) Interface with other Organizations

Coordinated with AWRP PDTs who have been receiving the national 3-D mosaic products on the transition to the new system. Sent the PDT users from NCAR and ESL the documentation for the new 3-D mosaic domain and new 3-D mosaic product suites. Established access for users to receive (via LDM) and to retrieve (via FTP) data in real-time from the new system.

e) Activity Schedule Changes

None.

Merging the Current Icing Potential and Polarimetric Hydrometeor Classification Algorithms

Edward A. Brandes and Kyoko Ikeda

National Center for Atmospheric Research

31 March 2006

1. Introduction

This planning document represents a first step in the development of a high-resolution polarimetric radar-based product specifically designed for detecting winter weather hazards and icing conditions. While polarimetric radar capabilities for discriminating among hydrometeor types are emphasized, it is recognized that hazard designations generally improve when all available information is considered. For example, accurate nowcasts of freezing-rain or freezing-drizzle conditions in the terminal area with radar requires knowing that the radar returns are from liquid precipitation and that temperatures are below freezing. In addition to radar measurements, the envisioned hazard detection product will incorporate the temperature interest field of the Current Icing Potential (CIP) algorithm, observed and forecast atmospheric soundings, surface observations, and satellite products developed by NASA. Requisite data streams are all currently available. For development purposes we use datasets collected previously during several field programs. The principal platform for development and display is the current polarimetric hydrometeor classification algorithm (HCA). Ultimately, hazard designations can be transported to the Weather Support to Deicing Decision Making (WSDDM) system and the planned high-resolution CIP system. We anticipate initial testing of the Winter HCA during the planned field program in Oklahoma.

2. Polarimetric radar measurements and potential HCA improvements

Polarimetric radars have distinct advantages over current operational systems that measure only radar reflectivity and components of the Doppler (radial velocity) spectrum. The added measurements should result in the improvement of several existing weather hazard algorithms and the development of new products (Table 1). All radar-based weather hazard products will benefit from improved hardware calibration and an enhanced capability to detect non-meteorological scatterers such as birds, insects, and ground echoes. Other capabilities include improved detection of freezing levels and melting layers. The measurements support sophisticated algorithms for discriminating between liquid and solid precipitation and for estimating raindrop sizes. It is possible to discriminate between frozen hydrometeor types, for example, snow crystals and snow pellets.

While the first-generation hydrometeor classification algorithms have sparked considerable interest, improvements can be made (Table 2). One of the more important inputs to the HCA is the freezing level. Atmospheric soundings are routinely made at 12-h intervals. This can be woefully inadequate whenever meteorological conditions vary

significantly in time and space. Forecast temperature profiles are available from numerical forecast models (e.g., RUC). However, the profiles are subject to error, especially when the weather changes rapidly. Poor temperature information can cause spurious HCA designations. Polarimetric measurements can be used to estimate freezing levels with an accuracy of ~150 m. By adjusting numerical model temperature profiles to match radar-derived freezing levels, bogus HCA classifications, such as rain layers above the freezing level, can be corrected and the expected vertical continuity of hydrometeor types assured.

The current HCA frequently makes supercooled-water designations at storm tops. While the upper regions of storms are favored icing locations, weak radar signals, low signal-to-noise ratios, and radar sidelobes could corrupt the measurements and negatively impact the HCA designations. The number of false icing designations can be reduced by weighing the climatological relationship between temperature and icing frequency used by the CIP algorithm, thereby eliminating situations that are too cold for significant icing. Also, we intend to evaluate the utility of the NASA icing product for eliminating false cloud top icing designations. The utility of a designated hazard would normally increase when both radar and satellite systems indicate icing conditions.

The remote designation of freezing rain and drizzle in the terminal area requires that surface temperatures be known. The needed data can be acquired either from meteorological observations or the RUC forecast model. To improve the discrimination between drizzle and light snow we intend to make use of the statistical texture properties of radar reflectivity measurements determined in a recent study conducted by the IFIPDT and extend that study for polarimetric measurements.

Finally, the current HCA designates the most likely hydrometeor type. A more realistic approach regarding icing hazards may be to account for the uncertainty in the radar measurements and simply designate icing risks as none, low, moderate, and high.

3. Other icing hazard detection enhancements (longer term)

Discussion with IFIPDT members disclosed additional ways that radar measurements could improve the designation of icing hazards. Freezing drizzle events often associate with shallow cloud layers which are capped by strong wind shear layers. At Denver International Airport drizzle typically occurs with low-level winds from the north-northeast. At about 1.5 km AGL the wind direction shifts to the southwest. The shear layer between the two wind regimes marks the top of the likely icing layer. Icing hazards are increased if there is enhanced upslope and an associated rapid generation of supercooled water in the lower wind layer. Both wind shear and upslope conditions should be diagnosable with Doppler measurements.

Freezing rain often associates with high liquid water contents and large drop sizes. Icing hazards can be significant because supercooled water may run along the wing before freezing on surface areas that are not protected from icing. Polarimetric radar should give improved estimates of liquid water contents, enable estimates of median drop sizes in freezing rain situations, and, consequently, support improved quantification of the icing threat.

The current CIP algorithm designates convective icing hazards by incorporating observations from the national lightning network. Lightning is a good indicator of strong

convective updrafts and, hence, possible icing conditions. Electric fields generated by thunderstorms can alter the orientation of frozen hydrometeors. Affected particles can be detected by polarimetric radar. The signal, a lightning precursor, appears most prominently in the differential propagation phase measurement. In addition, strong updrafts create strong wind divergence at storm top. The location of the updraft can be precisely determined by matching radial velocity divergence patterns near storm top with reflectivity maxima. A Convective Storm Top Algorithm could be developed. Capabilities for lightning detection and locating convective storm tops could be incorporated into the CIP algorithm. The storm top work would also be done in collaboration with the Turbulence PDT because of the severe turbulence that often occurs near thunderstorm tops.

TABLE 1: Improvement areas and new products likely with polarimetric measurements.

1) Hardware calibration
2) Discrimination of ground clutter and anomalous propagation
3) Discrimination of insects and birds
4) Hail detection
5) Liquid and solid precipitation quantification
6) Hydrometeor classification
7) Freezing-level and melting-layer designation
8) Detection of lightning precursors
9) Estimation of precipitation-impacted visibility

TABLE 2: Proposed enhancements to the current Hydrometeor Classification Algorithm

1) Upgrade consistency checks of HCA designations in the vertical and horizontal.
2) Add local correlation between reflectivity and differential reflectivity to improve rain/snow discrimination and for detecting possible icing conditions.
3) Add textural characteristics of reflectivity fields to improve the discrimination between light snow and drizzle.
4) Acquire surface temperature information to aid rain/snow discrimination and enable the unambiguous designation of freezing-drizzle and freezing-rain conditions.
5) Automatically ingest RUC temperature profiles and implement an adjustment procedure to force conformity with radar-determined freezing levels.
6) Add CIP interest fields for temperature to prevent icing designations in regions where the likelihood is low because temperatures are too cold.
7) Determine storm regions where icing is unlikely.
8) Import NASA icing products to evaluate the likelihood of icing hazards at storm top.

A Statistical and Physical Description of Hydrometeor Distributions in Colorado Snow Storms Using a Video Disdrometer

EDWARD A. BRANDES[1], KYOKO IKEDA[1], GUIFU ZHANG[2],
MICHAEL SCHÖNHUBER[3], AND ROY M. RASMUSSEN[1]

[1]*National Center for Atmospheric Research, Boulder, Colorado*

[2]*University of Oklahoma, Norman, Oklahoma*

[3]*Joanneum Research, Graz, Austria*

February 2006

_____

Corresponding author address: Dr. Edward A. Brandes, National Center for Atmospheric Research, P.O. Box 3000, Boulder, CO 80307.
E-mail: brandes@ncar.ucar.edu

ABSTRACT

Hydrometeor distributions in winter storms along the front-range in eastern Colorado are studied with a two-dimensional video disdrometer. The instrument provides shape, size, and terminal velocity information for particles larger than about 0.4 mm. The dataset is used to determine the form of particle size distributions (PSDs) in winter storms and to search for useful inter-relationships among the governing parameters of assumed distribution forms and environmental factors. Snowfalls are dominated by almost spherical aggregates having near-exponential or super-exponential size distributions. Raindrop size distributions are more peaked than that for snow. A relation between bulk snow density and particle median volume diameter is derived. The data suggest that some adjustment may be needed in relationships found previously between temperature and the concentration and slope parameters of assumed exponential PSDs. A potentially useful relationship is found between the slope and shape terms of the gamma PSD model.

1. Introduction

Observations of particle size distributions in winter storms are needed to verify and improve microphysical parameterizations in numerical forecast models and to accurately quantify winter precipitation, discriminate among hydrometeor types, and develop algorithms for determining particle size distributions with remote sensors such as polarimetric radar. This study examines bulk characteristics of observed particle distributions using a two-dimensional video disdrometer. While designations of particle habits are possible using shape and terminal velocity information obtained with the disdrometer, this was not attempted because the dataset for some hydrometeor types is small. All measurements were obtained at ground. Obviously, factors other than surface conditions determine the characteristics of precipitation. Nonetheless, the examined dataset is representative of significant upslope snowfall events along the front-range in eastern Colorado.

We begin with a description of the disdrometer and analysis procedures. Instrument capabilities are demonstrated; and physical properties of winter precipitation, such as, particle bulk density, shape, terminal velocity, and snowfall rate are investigated. Inter-relationships among particle size distribution (PSD) parameters and relationships with environmental factors are examined, and implications for microphysical parameterization in numerical forecast models are discussed.

2. Data and analysis

Detailed technical descriptions of the disdrometer are given by Kruger and Krajewski (2002) and Thurai and Bringi (2005). The instrument consists of two horizontally-oriented line-scan cameras, separated in the vertical by about 6 mm, that provide orthogonal views of hydrometeors falling through a common 10×10 cm area. Blocked photo-detectors for each camera are recorded at a line scan frequency of 51.3 kHz. Horizontal resolution is approximately 0.15 mm. Vertical resolution depends on particle terminal velocity and is roughly 0.1–0.2 mm for raindrops and 0.03 mm for snowflakes. The instrument is calibrated by dropping spheres of known size into the device. Accurate determination of hydrometeor characteristics can be made for particles with dimensions greater than ~0.4 mm. Cloud-size particles are not resolved. Terminal velocities are determined from the time it takes a particle to break each camera plane and can be verified by comparing computed values for raindrops against published laboratory experiments.

Recorded information for each hydrometeor includes front and side silhouette images (Fig. 1), equivalent volume diameter, maximum width and height, an estimate of oblateness (valid for raindrops), and terminal velocity. A wealth of information regarding precipitation-size particles from numerous storm types and a variety of temperature and humidity conditions is readily obtained.

The disdrometer was installed at the National Center for Atmospheric Research Marshall Snowfall Test Site. Other instrumentation included thermometers, a hygrometer, anemometers, snow gauges, and a visibility sensor. Disdrometer measurements are influenced by the wind (Nešpor et al. 2000). Problems are exacerbated for snow particles because of their small terminal velocities. Wind-affected observations can be identified by the distribution of hydrometers within the viewing region and increased scatter among velocity estimates. To minimize wind effects, the disdrometer was placed within a wind shield. Analyses presented are

generally restricted to events with ambient wind speeds < 4 m s^{-1}. Our results may be biased if, for example, the production of large aggregates is hindered by strong wind and turbulence.

Particle distributions were fit with the exponential model (e.g., Marshall and Palmer 1948; Gunn and Marshall 1958)

$$N(D)=N_0\exp(-\varLambda D) \quad ,\tag{1}$$

where N_0 (units of mm^{-1} m^{-3}) is a concentration intercept parameter, $\varLambda$ (mm^{-1}) is a slope term, and D (mm) is the particle equivalent volume diameter. The observations were also fit with the gamma model (e.g., Ulbrich 1983)

$$N(D)=N_0 D^\mu \exp(-\varLambda D) \quad ,\tag{2}$$

where N_0 (mm$^{-\mu-1}$ m^{-3}) is now a number concentration parameter, μ is a distribution shape or curvature parameter, and $\varLambda$ (mm^{-1}) is a slope term sensitive to the larger particles. The governing parameters in (1) and (2) were estimated from the 3rd and 6th moments and the 2nd, 4th, and 6th moments of the observed particle distributions, respectively. Snow storm PSDs were generally computed for 5-min samples to ensure an adequate number of particles for each spectra. PSDs in rain storms were computed for 1-min samples to be consistent with previous studies. Typically, each spectrum contained hundreds to thousands of hydrometeors.

Once the PSD is known other parameters can be computed. The median volume diameter D_0 of the particles is defined

$$\int_0^{D_0} D^3 N(D)dD = \int_{D_0}^{D_{max}} D^3 N(D)dD \quad ,\tag{3}$$

where one-half of the precipitation volume is contained in particles smaller and one-half in particles larger than D_0 and D_{max} is the size of the largest observed particle in the distribution. The total number concentration N_T is

$$N_T = \int_0^{D_{max}} N(D)dD \quad ,\tag{4}$$

and the mean terminal velocity v_t is

$$v_t = \frac{\int_0^{D_{max}} N(D)v_{obs}(D)dD}{\int_0^{D_{max}} N(D)dD} \quad ,\tag{5}$$

where v_{obs} is the observed particle velocity. Other characteristic velocities can be computed, for example, by weighing each observation according to its volume or mass.

Precipitation characteristics for a long-lived snow event on November 20, 2004 are plotted in Fig. 2. Surface air temperatures for this event began at 0.6^{o}C, cooled to 0°C at 0645 UTC, and varied between 0°C and -3^oC afterwards. The top panel shows snowfall rate (water equivalent in mm h^{-1}) as measured with a weighing snow gauge having a resolution of 0.0254 mm and computed from disdrometer measurements using a density–size relation described in

section 3a. Other panels show D_0 and D_{max}, N_T, and v_t. In general, displayed parameters show fair stability from sample to sample and seemingly respond to meteorological factors as manifest by the independent gauge measurements. Increases in precipitation rate at 0915 and 1520 UTC exhibit corresponding increases in D_0 and D_{max} as well as temporary increases in total number concentration. The rate increase at 0915 UTC was marked by a significant decrease in particle terminal velocity. Relatively heavy snowfall rates after 2130 UTC do not show a significant increase in particle size but an order of magnitude increase in number concentration. Overall, the terminal velocity for this event is poorly correlated with other displayed variables.

Among characteristic velocities, mean values are the smallest because more numerous and slower-falling small particles have the same weight as less plentiful and faster-falling large particles. Mass-weighted terminal velocities are slightly less than volume-weighted velocities because mass increases more slowly than volume as the particle diameter increases.

The gamma distribution has been widely accepted by the meteorological radar community for raindrops because it readily describes a variety of observed distributions while maintaining a simple and efficient functional form. Application to snowflakes needs some justification. Modelers and observationalists often assume that particles in winter storms are exponentially distributed. Figure 3 presents PSD examples from a snow event on March 18, 2003. The turn down at the smallest size in the top panel is regarded to be a detection problem. Fitted relations for truncated-exponential and truncated-gamma distributions are overlaid. Computed properties and governing parameters for the two PSD models are summarized in Table 1. Perusal of Fig. 3 reveals that the gamma distribution gives a better representation of distributions that are nonlinear, i.e., the upward curving distribution of 2125–2130 UTC and downward curving distribution of 2230–2235 UTC. Estimates of N_0 and Λ with the two models show considerable temporal variation.

The frequency of the gamma PSD shape factor μ differs for winter rain and snow storms (Fig. 4). The distribution for snow is skewed with a mode of +1 or close to exponential. A number of μs are negative, an indication that small particle concentrations exceed that of an exponential distribution. Negative μs are frequently seen in aircraft observations (e.g., Heymsfield et al. 2002). The mean value for winter rain is roughly 5. While these values could be used to define a special gamma distribution with a constant μ, that could lead to significant error if the total particle concentration, coalescent, or the evaporative properties of the distribution are desired.

Figure 5 presents a time series of D_0 and D_{max}, estimates of μ, assuming a truncated-gamma PSD, and Λ and N_T for both truncated-gamma and truncated-exponential PSDs. The data are for an event on November 1, 2004 during which precipitation began as rain, became mixed-phase, and finally changed to snow. Snowfall rates varied between 0.5 and 6 mm h^{-1}. Temperatures fell from 4°C at 0000 UTC to -1°C at 0500 UTC. The average gamma-PSD shape parameter for the rain stage, computed for 1 min samples, is ~3. The shape parameter decreases to negative values as precipitation begins to change to snow (0045 UTC). Negatives arise from a combination of a few relatively large wetted snowflakes and large numbers of small raindrops and ice particles which are narrowly distributed. The shape factor increases to about 0 between 0145 UTC and 0315 UTC and then averages between -1 and -2. There is little correlation between μ and D_{max} and the μ and Λ traces are quite stable from sample to sample. This suggests that, except perhaps for the early mixed-phase period, the negative μs are real and not the result of some sampling issue. Whenever μ is negative, the slope of the truncated-exponential PSD is larger than that of the truncated-gamma PSD.

The truncated-exponential PSD overestimates particle total number concentration for rain and tends to underestimate the concentration for mixed-phase and snow portions of the storm (Fig. 5, lower panel). The exponential model is a poor fit during the mixed-phase stage and for some spectra the procedure used to compute the PSD governing parameters does not converge to a solution. The truncated-gamma distribution overestimates the concentration for negative μ. This could be a detection problem with the disdrometer or a truncation problem with the gamma model. For the most part, disdrometer observations of N_T lie between estimates for the truncated-exponential and truncated-gamma PSDs. However, the gamma model provides a much better fit to hydrometeor distributions during the rain and mixed-phase portions of the event.

3. PSD physical attributes

a. Bulk density

A critical issue for estimating liquid equivalents and for quantifying PSD attributes with polarimetric radar measurements is the relation between particle size and density. To compute density, snowflake volumes were determined by revolving components of the two silhouette images and then finding the geometric mean of the two estimates. Bulk snow density (ρ_s) was determined for 5-min samples from the disdrometer-derived precipitation volume and gauge-measured precipitation mass. Sensitivity to the number of particles, calculated volumes for often highly-irregular particle shapes, and gauge quantization at low precipitation rates, dictates that density estimates are only approximate. However, density calculations for intense summer rain events average close to 1 g cm^{-3}, indicating that the method has some merit.

Figure 6a shows the relation between ρ_s and particle median volume diameter. Although it is not shown, data points from specific days tend to cluster, attesting to the importance of meteorological conditions and indicating domination by aggregates or snow pellets and whether riming is light or heavy.

The overlaid curve, a least-squares fit applied in an attempt to determine a climatological relation, is given by

$$\rho_s(D) = 0.178 D_0^{-0.922} \quad , \tag{6}$$

where D_0 is in mm and ρ_s is in g cm^{-3}. This expression is very similar to the inverse linear relation $\rho_s = 0.17 D^{-1}$ found by Holroyd (1971) for Great Lakes snow storms and to an intermediate relation $\rho_s = 0.15 D^{-1}$ determined by Fabry and Szyrmer (1999) from a literature survey. A relation for snow particle mass m (in grams) corresponding to (6) is

$$m(D) = 8.90 \times 10^{-5} D_0^{2.1} \quad . \tag{7}$$

Equation (6) does not match the observations very well at small median volume diameters. In truth, the disdrometer does a poor job of measuring small snow particles. Note that there are no observations with $D_0 < 0.6$ mm. Hence, Eq. (6) probably gives a better representation of small snowflake density than implied by the disdrometer observations. With (6) PSDs characterized by $D_0 < 1$ mm have densities > 0.20 g cm^{-3}. Zikmunda and Vali (1972) found that for particles with diameters of 1.0–2.0 mm densities were 0.45–0.25 g cm^{-3}. Our

relation gives 0.18–0.09 g cm^{-3}, a factor of 2.5 less. Our values are fairly close to that found by Locatelli and Hobbs (1974) for lump graupel. Densities with (6) are larger than those of Muramoto et al. (1995; their Fig. 7) for small snowflakes but in agreement for large flakes. The video disdrometer probably underestimates the contribution of the smaller particles to the total precipitation volume; hence, our bulk densities could be overestimated. The density–size relation of Magono and Nakamura (1965) for large snowflakes predicts a density of 0.08 g cm^{-3} for a diameter of 5 mm and a density of 0.02 g cm^{-3} for a diameter of 10 mm. Densities with (6) are 0.04 g cm^{-3} and 0.02 g cm^{-3}, respectively, and are in rough agreement with those of Muramoto et al. The wide range in reported density values probably reflects both precipitation climatology and how snowflake volumes were computed.

In the top panel of Fig. 2, snowfall rates computed by multiplying the volume of individual particles by Eq. (6) densities are compared with the snow rate measured with a gauge. Overall, the comparison is good; but significant differences occur for the heavier snow rate after 2000 UTC. Snow particles during this storm stage may be more dense than given by (6). Particle sizes are relatively small for this stage suggesting that a significant number of particles may not have been detected. Until verified by additional datasets, the density relation should be used cautiously.

Particle bulk density is plotted against surface temperature in Fig. 6b. There is a tendency for low densities to be more frequent as temperatures warm above –5°C. This is undoubtedly a consequence of increased aggregation. Figure 6c examines the relationship between bulk density and relative humidity. A tendency is also evident for the frequency of low-density aggregates to increase as humidity increases. This is expected because high humidity fosters particle growth by aggregation (Hosler et al. 1957). Relationships with temperature and humidity are weak. Undoubtedly more than surface conditions determine bulk density.

b. Aggregate axis ratios

In order to discriminate between particle habits with polarimetric radar, mean particle shapes must be known. Aspect ratios of raindrops and pristine ice crystals are well known. Less is known about the mean shape of aggregates which dominate surface precipitation. Axis ratios, defined here as r the ratio of the maximum vertical dimension divided by the maximum horizontal dimension, are illustrated in Fig. 7. While this ratio differs from that obtained by fitting the images with ellipses and dividing the minor axis by the major axis, the current definition allows comparison with radar measurements of differential reflectivity in a statistical sense. Axis ratio scatter is large for small particles. Some of the scatter, particularly at the smallest sizes, probably stems from instrument sensitivity. Large ratios associate with aggregates whose axis of elongation is closer to vertical than horizontal. Many small particles with small axis ratios are stellar crystals much like that seen in the lower right panel of Fig. 1. The scatter in axis ratios decreases as size increases, and the particles become more spherical on average.

The curve in Fig. 7 is a fit applied to modal values of axis ratios for 0.2 mm size bins. For the event shown, axis ratios increase slightly with size from 0.9 to 1.0. The usual case for aggregates seems to be a flat distribution with an axis ratio near 1.0. This is consistent with the finding of Magono and Nakamura (1965) who show aggregates to be largely spherical on average (their Fig. 2).

Appendix 2   7

c. Terminal velocity

Examples of observed particle terminal velocities for a storm on March 5, 2004 are given in Fig. 8. The upper panel shows mixed-phase precipitation detected between 0100 and 0115 UTC. The temperature fell from 5.5 °C to 0.5°C during the period. Raindrops, ice pellets, and wetted aggregates were observed. From 0145 to 0200 UTC the temperature was ~0.1°C (middle panel). Hydrometeor habits were dendrites, plates, stellars, and aggregates of these forms. During this stage terminal velocities were weakly dependent on size, varying from about 0.8 m s^{-1} for a particle with an equivalent volume diameter of 1 mm to 1.1 m s^{-1} for a particle with a diameter of 11 mm. Observed velocities for larger particles are within 0.1 m s^{-1} of that reported by Locatelli and Hobbs (1974) for un-rimed aggregates (their Fig. 20). Between 0220 and 0235 UTC the temperature lowered to −0.5 °C. Hydrometeor habits were classified by an observer as irregular snow particles and lump graupel. Comparison with relations of Locatelli and Hobbs shows the observed terminal velocities to be slightly higher than their densely rimed aggregates but not as high as their low density graupel. The temporal variation in the size−terminal velocity relation seen in Fig. 8 is typical of winter storms along the front-range.

Inter-relationships among mass-weighted terminal velocity, size (D_0), and ambient temperature for a number of storms are illustrated in Fig. 9. Individual data points are color coded for density. Small, high density particles with terminal velocities >1.2 m s^{-1} (Fig. 9a) are indicative of small lump graupel or snow pellets (Zikmunda and Vali 1972; Locatelli and Hobbs 1974). Large, less dense particles are aggregates. Terminal velocities of these particles closely match that found by Locatelli and Hobbs for aggregates. Fall speeds for aggregates increase slowly with size in spite of the decrease in particle density. This result is similar to that of Locatelli and Hobbs who found that aggregates fall faster than their constituents. The terminal velocity for spherical snowflakes can be computed (Pruppacher and Klett 1997) as

$$v_t = \left(\frac{4 g \rho_s D}{3 C_D \rho_a} \right)^{0.5} \quad , \tag{8}$$

where g is the acceleration of gravity, C_D is the drag coefficient, and ρ_a is the density of air. Fall velocities increase as particle density and size increases and decrease as the drag coefficient increases. Particle bulk density and size are inversely related [e.g., Eq. (6)]. Because bulk density varies according to $D^{-0.922}$, the terminal velocity is a little more sensitive to D than ρ_s. Their product increases slowly as D increases. This could partly explain the increase in terminal velocity seen for large aggregates. Drag coefficient impacts have not been investigated. Magono and Nakamura (1965) determined the drag coefficient for dry snow particles was near constant. Fall speeds could increase if the drag coefficient decreased with particle size. Intuitively, we expect drag to increase for large fluffy aggregates.

There is a relationship between terminal velocity and temperature (Fig. 9b). As temperatures warm above about −5°C, fall speeds increase noticeably from about 0.9 m s^{-1} to 1.3 m s^{-1}. The increase, seen for all density categories, must be related to aggregation and corresponding increases in particle size. The relation between particle median volume diameter and temperature is presented in Fig. 9c. Our dataset is limited but as temperature increases above −7°C or so, aggregation becomes ever more active and the spread in particle median volume diameters increases. Hosler et al. (1957) found a temperature of −4°C and Hobbs et al. (1974) found a temperature of −5°C as the point at which particle stickiness increases and

aggregation is enhanced. Largest D_0s in our dataset were at temperatures $>-1^oC$. This agrees with the findings of Hobbs et al. They also found a secondary dendritic growth region in the temperature range -12^oC to -17^oC. Unfortunately, the dataset collected to date has too few observations in this temperature range to verify this finding.

d. Snowfall rate

Snowfall rate (*S*, liquid equivalent) and bulk density in winter precipitation are inversely related (Fig. 10a).[1] This is not surprising given that heavy snowfall rates are often characterized by aggregates and warmer temperatures. Heavy rates with dense pristine ice crystals or snow pellets simply were not observed. Snowfalls with very light rates and very low bulk densities were seldom observed. Perhaps there are too few particles at low precipitation rates to grow large aggregates.

Expectedly, snow particle terminal velocity and snowfall rate are related (Fig. 10b). Most of the data points at light snowfall rates are aggregates and have a terminal velocity of ~1 m s^{-1}. On site particle observations support the notion that data points with light snowfall rates and relatively high v_t are snow pellets or lump graupel. The increase in mass-weighted terminal velocity at high snow rates for aggregates is believed to arise primarily from an increase in particle size (Fig. 10c). For the Colorado Front Range the most common situation appears to be a snowfall rate of about 1 mm h^{-1} and a D_0 on the order of 1.5 mm.

For low snow rates there is no obvious relation with the shape parameter of the gamma PSD (Fig. 10d). The curvature term varies considerably from small negative values to more than 5. Although the sample size is small, heavy snow rates tend to be slightly super-exponential. Accompanying high number concentrations probably result from the rapid production of small particles.

4. Numerical model microphysics parameterization

Some numerical forecast models incorporating second or higher moment particle size distributions such as (1) and (2) close the system of unknowns by forecasting the precipitation mass and incorporating empirical relationships between the governing parameters of the distribution and temperature. Disdrometer-derived values of N_0 for storms in Colorado, assuming a truncated-exponential PSD, are plotted against temperature in Fig. 11 (upper panel). A fit to the data is

$$N_0 = 7\times10^3(T_0 - T)^{0.6} \quad , \tag{9}$$

where $T_0 = 273.15$ K and T is the observed temperature (K). Also, shown is a relationship used by Hong et al. (2004) and Thompson et al. (2004)

$$N_0 = 2\times10^3 \exp[0.12(T_0 - T)] \quad , \tag{10}$$

that was derived from observations described by Houze et al. (1979). The dataset of Houze et al. consists of 37 spectra obtained at temperatures of -42^oC to 6^oC from 4 winter storms in the state

---

[1] All data points with snowfall rates > 4 mm h^{-1} are from the same storm.

of Washington. The particle sensor had a measurement resolution of 70 μm and a data window width of 1050 μm. In general, particle sizes would have been estimated from the shape of partial images. Houze et al. truncated the size distribution on the small end when the data departed from an exponential distribution.

For the most part, our N_0s are larger than that found by Houze et al. (1979). While differences in instrumentation and data processing may contribute to this result, particle distributions in Colorado may simply be narrower, having higher concentrations of small particles and fewer large particles, than those in the Pacific Northwest. Figure 11 suggests a marked decrease in the intercept parameter as temperatures warm above –5°C and aggregation broadens the distribution. This conclusion is supported by a corresponding decrease in Λ (Fig. 11, lower panel). The fitted $\Lambda-T$ relation is

$$\Lambda = 2.27(T_0 - T)^{0.18} \quad . \tag{11}$$

A corresponding fit to the data of Houze et al. is

$$\Lambda = 1.0 + 0.1(T_0 - T) \quad . \tag{12}$$

Houze et al. determined correlation coefficients of –0.66 between temperature and N_0 and –0.90 between the slope of the exponential PSD and temperature. Correlation coefficients for the disdrometer observations are much smaller in magnitude. Although correlation could be improved by averaging over periods longer than 5 min, the coherence seen in our data from sample to sample (e.g., Figs. 2 and 5) suggests the fluctuations are largely meteorological.

Figure 12 shows concentration parameters for truncated-exponential and truncated-gamma PSDs plotted against snowfall rate. Snowfall rates were determined with a gauge, and the N_0s were computed from disdrometer observations. A fit to the data yields

$$N_0 = 5 \times 10^3 S^{-1.2} \quad . \tag{13}$$

For light snowfall rates ($S < 2$ mm h^{-1}) the concentration parameter for the truncated-exponential distribution varies by two orders of magnitude. Although the dataset is limited and largely from one storm, there is close agreement between the observations and (13) for $S > 2$ mm h^{-1}. Sekhon and Srivastava (1970) determined N_0 and S were related by

$$N_0 = 2.50 \times 10^3 S^{-0.94} \quad . \tag{14}$$

This relation, used by Reisner et al. (1998) in their numerical model microphysical parameterization scheme, is plotted in Fig. 12. The relation agrees quite well with that determined here.

N_0s for the truncated-gamma PSD are plotted versus S in the lower panel of Fig. 12. A fit to the data is

$$N_0 = 1.3 \times 10^4 S^{-1.45} \tag{15}$$

10

Increased scatter, attributed to greater freedom when fitting the observed particle distributions with a three-parameter model, would seem to preclude the utility of (15).

Relationships between the shape and slope parameters, assuming truncated-gamma PSDs, are shown in Fig. 13. Fitted relations for snow, rain, and mixed-phase precipitation are

$$\mu = -0.00499\Lambda^2 + 0.798\Lambda - 0.666 \quad , \tag{16}$$

$$\mu = -0.00152\Lambda^2 + 0.684\Lambda - 1.95 \quad , \text{ and} \tag{17}$$

$$\mu = -0.000120\Lambda^2 + 0.602\Lambda - 2.06 \quad . \tag{18}$$

Large μ and Λ are characteristic of narrow PSDs and commonly occur at the beginning and ending of events when small numbers of small particles are observed. Hence, computed values tend to be noisier during these storm stages. Caution should be exercised when using relationships such as (16)–(18) because, as noted by Chandrasekar and Bringi (1987), derived PSD attributes can be highly correlated due to errors in the computation of particle moments. The issue is discussed further by Zhang et al. (2003) who argue that, although observational error does contribute to correlation between derived PSD properties, the derived relations contain useful meteorological information. Seifert (2005) conducted a study with a stochastic drop breakup/coalescence model that suggests relations similar to (16)–(18) represent fundamental properties of drop distributions in convective storms. Hence, a physical relationship is believed to exist between these two parameters. Such a relationship may be useful when a two-parameter PSD model is needed.

As in Fig. 4, PSDs for heavy snow events tend to be broad and often closer to exponential than that for winter rains (Figs. 13a,b). For a particular μ, however, Λ for snow tends to be smaller than that for rain. Consequently, the fitted relation slope for snow is larger than that for rain, especially for heavier precipitation events. The dataset for mixed-phase precipitation (Fig. 13c) is relatively small but indicates a distribution somewhat intermediate between snow and rain.

5. Summary and discussion

The video disdrometer is a powerful observational tool for studying the microphysical properties of winter storms. What the instrument lacks in resolution is made up by the sheer volume of observations readily obtained for precipitation-sized particles in a variety of storms and under different meteorological conditions. The observations should prove important for verifying and developing microphysical parameterizations in numerical forecast models and for the interpretation of polarimetric radar observations.

Our results show that while PSDs in winter storms are close to exponential there are often significant departures from this form and, hence, benefits for modeling the distributions with a gamma distribution. However, the advantage with the gamma distribution is largely the capability to handle distributions of mixed-phase particles and the raindrop populations that stem from melting. The gamma model adds complexity to a numerical model because another parameter is introduced. However, the existence of relationships between μ and Λ, as in Fig. 13, is important because it effectively reduces the three-parameter gamma distribution to two

parameters. Consequently, it should not be necessary to impose severe assumptions on the PSD such as a constant μ.

Using precipitation volume measurements from the disdrometer we derived a relationship for bulk density [Eq. (6)] that is an almost inverse linear relation with particle size. Although the correlations are weak, further refinement of the relation may be possible by considering the influence of temperature and humidity on snowflake density.

Heavy snow rates along the front-range in eastern Colorado typically involve relatively warm temperatures and aggregates with large median volume diameters. The increase in snow volume more than offsets the reduction in bulk density as particles grow in size. Heavy snow rates are also supported by increases in particle terminal velocity. The shape parameter of the gamma distribution model in heavy snows is often negative, indicating the presence of super-exponential concentrations of small particles. Negative μs can be a problem when using the gamma model to calculate N_T. Negative μs can be a problem when using the gamma model to calculate N_T. To avoid an infinite or unrealistic N_T, the distribution can be truncated at a small drop size D_{min}. For remote sensing N_T is not an overly important issue because its correlation with radar measurements is relatively low. The problem is greater for a two-moment numerical model that predicts N_T and then uses it to derive other variables. A solution may be to develop a parameterization scheme for N_T based on predictions of precipitation mixing ratio and radar reflectivity.

Empirical relationships between temperature and the concentration and slope parameters of the exponential PSD were evaluated. At a specific temperature N_0 varied by an order of magnitude, and the range in Λ was broad. Over the temperature range of -20°C to -5°C a small decrease in the magnitude of both parameters was noted. Over the range -5°C to 0°C N_0 and Λ decrease markedly as aggregation broadened the PSD. Observed N_0s and Λs were larger than in the Pacific Northwest, suggesting that PSDs in Colorado are narrower and composed of smaller particles. N_0 and snowfall rate S are weakly correlated at snowfall rates < 3 mm h^{-1} with N_0 varying by more than two orders of magnitude. Hence, the relation does not appear to be useful.

This study emphasized bulk characteristics of storms. Future efforts will include detailed studies of particle evolution within winter storms. Of particular interest are the conditions that determine whether or not significant aggregation takes place. Also, as the dataset grows, inter-relationships between variables described here will be refined and habit-specific relations will be developed. Hydrometer properties such as bulk density and terminal velocity are clearly determined by more than size. A "fuzzy logic" approach may prove useful when the theoretical form of the relation is not known but inter-relationships among bulk attributes of particle distributions and their dependence on environmental factors such as temperature and humidity are desired.

REFERENCES

Brandes, E. A., G. Zhang, and J. Vivekanandan, 2002: Experiments in rainfall estimation with a polarimetric radar in a subtropical environment. *J. Appl. Meteor.,* **41,** 674–685.

Chandrasekar, V., and V. N. Bringi, 1987: Simulation of radar reflectivity and surface measurements of rainfall. *J. Atmos. Oceanic Technol.,* **4,** 464–478.

Fabry, F., and W. Szyrmer, 1999: Modeling of the melting layer. Part II: Electromagnetic. *J. Atmos. Sci.,* **56,** 3593–3600.

Gunn, K. L. S., and J. S. Marshall, 1958: The distribution with size of aggregate snowflakes. *J. Meteor.,* **15,** 452–461.

Heymsfield, A. J., A. Bansemer, P. R. Field, S. L. Durden, J. L. Stith, J. E. Dye, W. Hall, and C. A. Grainger, 2002: Observations and parameterizations of particle size distributions in deep tropical cirrus and precipitating clouds: Results from in situ observations in TRMM field campaigns. *J. Atmos. Sci.,* **59,** 3457–3491.

Hobbs, P. V., S. Chang, and J. D. Locatelli, 1974: The dimensions and aggregation of ice crystals in natural clouds. *J. Geophys. Res.,* **79,** 2199–2206.

Holroyd, E. W., III, 1971: The meso- and microscale structure of Great Lakes snowstorm bands: A synthesis of ground measurements, radar data, and satellite observations. Ph.D. dissertation, State University of New York at Albany, 148 pp.

Hong, S.-Y., J. Dudhia, and S.-H. Chen, 2004: A revised approach to ice microphysical processes for the bulk parameterization of clouds and precipitation. *Mon. Wea. Rev.,* **132,** 103–120.

Hosler, C. L., D. C. Jensen, and L. Goldshlak, 1957: On the aggregation of ice crystals to form snow. *J. Meteor.,* **14,** 415–420.

Houze, R. A., P. V. Hobbs, P. H. Herzegh, and D. B. Parsons, 1979: Size distributions of precipitation particles in frontal clouds. *J. Atmos. Sci.,* **36,** 156–162.

Kruger, A., and W. F. Krajewski, 2002: Two-dimensional video disdrometer: A description. *J. Atmos. Oceanic Technol.,* **19,** 602–617.

Locatelli, J. D., and P. V. Hobbs, 1974: Fall speeds and masses of solid precipitation particles. *J. Geophys. Res.,* **79,** 2185–2197.

Magono, C., and T. Nakamura, 1965: Aerodynamic studies of falling snowflakes. *J. Meteor. Soc. Japan,* **43,** 139–147.

Marshall, J. S., and W. McK. Palmer, 1948: The distribution of raindrops with size. *J. Meteor.,* **5,** 165–166.

Muramoto, K.-I., K. Matsuura, and T. Shiina, 1995: Measuring the density of snow particles and snowfall rate. *Electronics and Communications in Japan,* Part 3, **78,** 71–79. Translated from Denshi Joho Tsushin Gakkai Ronbunshi, 77-D, 1994, 2353–2360.

Nešpor, V., W. F. Krajewski, and A. Kruger, 2000: Wind-induced error of rain drop size distribution measurement using a two-dimensional video disdrometer. *J. Atmos. Oceanic Technol.,* **17,** 1483–1492.

Pruppacher, H. R., and J. D. Klett, 1997: *Microphysics of clouds and precipitation.* Kluwer Academic, 954 pp.

Reisner, J., R. M. Rasmussen, and R. T. Bruintjes, 1998: Explicit forecasting of supercooled liquid water in winter storms using the MM5 mesoscale model. *Quart. J. Roy. Meteor. Soc.,* **124,** 1071–1107.

Seifert, A., 2005: On the shape–slope relation of drop size distributions in convective rain. *J. Appl. Meteor.,* **44,** 1146–1151.

Sekhon, R. S., and R. C. Srivastava, 1970: Snow size spectra and radar reflectivity. *J. Atmos. Sci.,* **27,** 299–307.

Thompson, G., R. M. Rasmussen, and K. Manning, 2004: Explicit forecasts of winter precipitation using an improved bulk microphysics scheme. Part I: Description and sensitivity analysis. *Mon. Wea. Rev.,* **132,** 519–542.

Thurai, M., and V. N. Bringi, 2005: Drop axis ratios from 2D-video disdrometer. *J. Atmos. Oceanic Technol.,* **22,** 966–978.

Ulbrich, C. W., 1983: Natural variations in the analytical form of the raindrop size distribution. *J. Appl. Meteor.,* **22,** 1764–1775.

Zhang, G., J. Vivekanandan, E. A. Brandes, R. Menegini, and T. Kozu, 2003: The shape–slope relation in observed gamma drop size distributions: Statistical error or useful information? *J. Atmos. Oceanic Technol.,* **20,** 1106–1119.

Zikmunda, J., and G. Vali, 1972: Fall patterns and fall velocities of rimed ice crystals. *J. Atmos. Sci.,* **29,** 1334–1347.

TABLE 1. Computed PSD attributes for the distributions in Fig. 2. Fitted values are presented for truncated particle size distributions. C_T is the number of particles observed in the 5-min interval. Gauge-observed snowfall rates S (liquid equivalents) are also shown. Units are: N_T, $m^{-3}\ mm^{-1}$; N_0, $m^{-3}\ mm^{-\mu-1}$; D_0, mm; Λ, mm^{-1}; and S, $mm\ h^{-1}$. Times are UTC.

Time interval	2050–2055	2125–2130	2230–2235
N_T	1.16×10^3	1.89×10^2	3.68×10^3
C_T	3010	564	11914
D_0	1.79	6.37	2.09
N_0 (gamma)	1.39×10^3	7.18×10^1	2.33×10^4
μ (gamma)	−0.90	−0.78	2.09
Λ (gamma)	1.40	0.35	2.25
N_0 (exponential)	1.91×10^3	1.82×10^1	1.85×10^4
Λ (exponential)	1.80	0.35	1.77
S	2.70	2.59	3.03
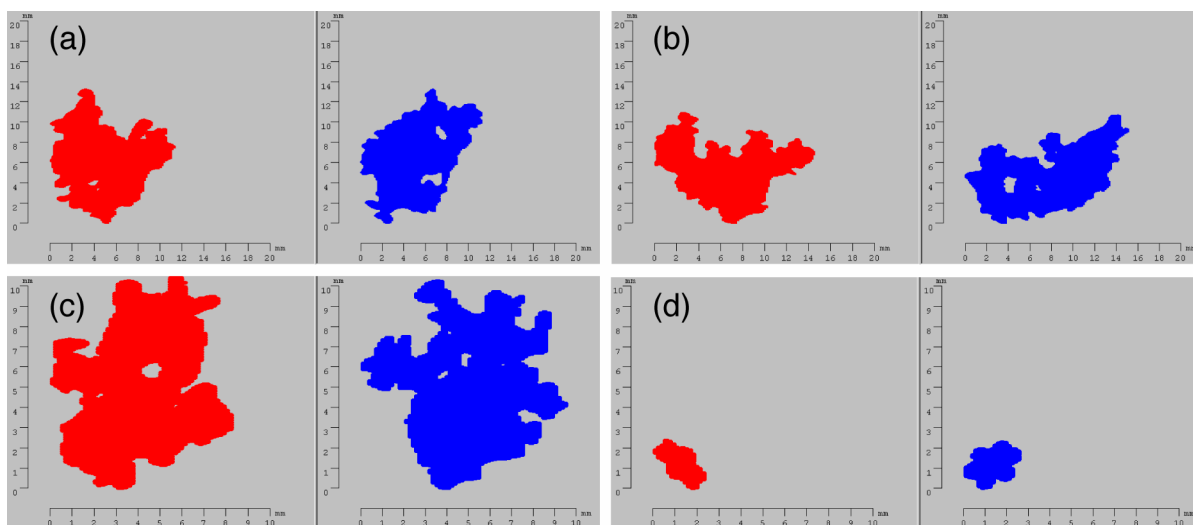
FIG. 1: Sample video disdrometer images. Front and side profiles are shown. Size increments are in 2 mm in panels (a) and (b) and 1 mm in panels (c) and (d).
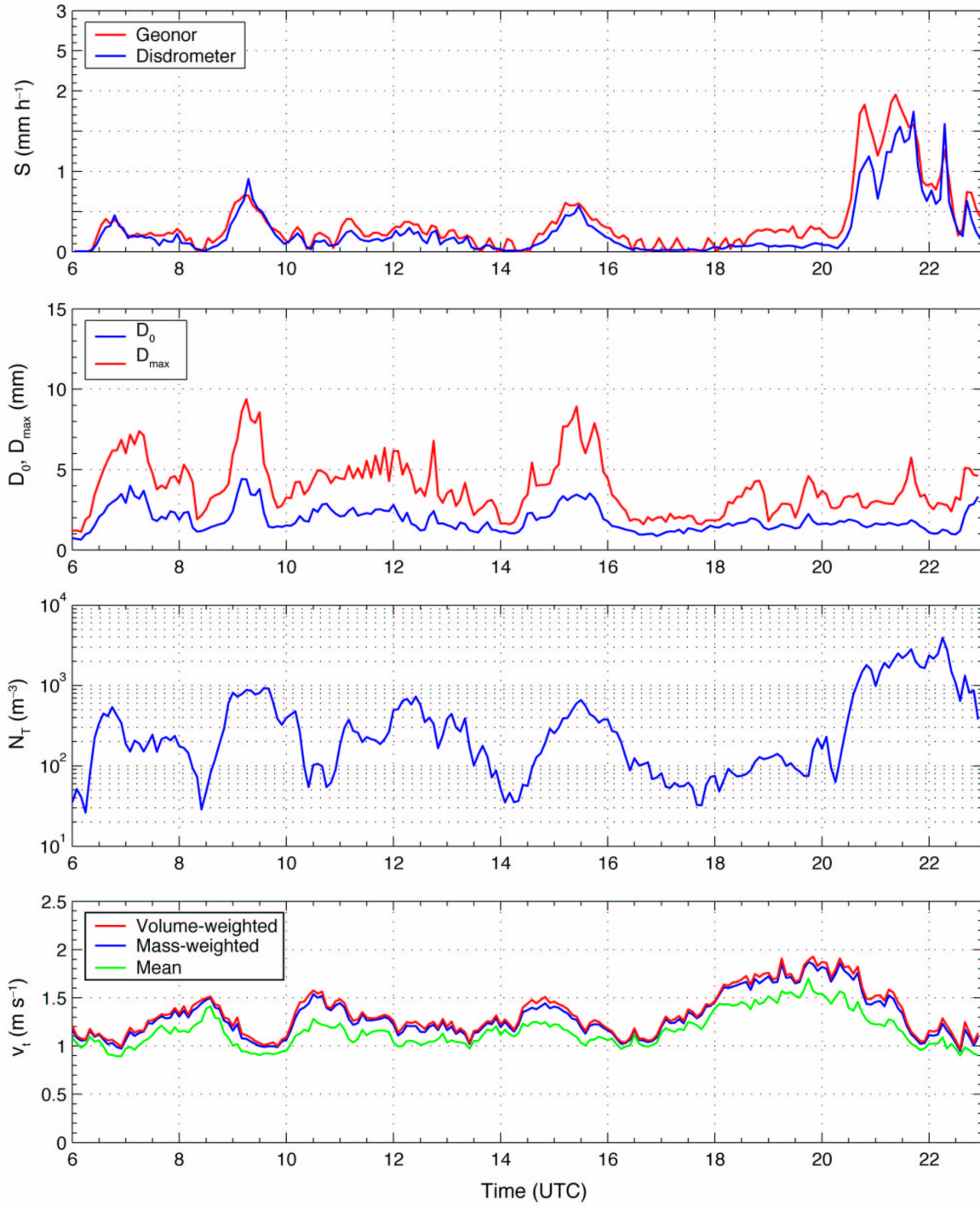
FIG. 2: Time series of observed PSD attributes computed for a storm on 20 Nov 2004. Snow rate S as computed from disdrometer observations and measured by a shielded snow gauge, median volume diameter D_0 and maximum particle size D_{max}, total number concentration N_T, and characteristic terminal velocities v_t are shown.
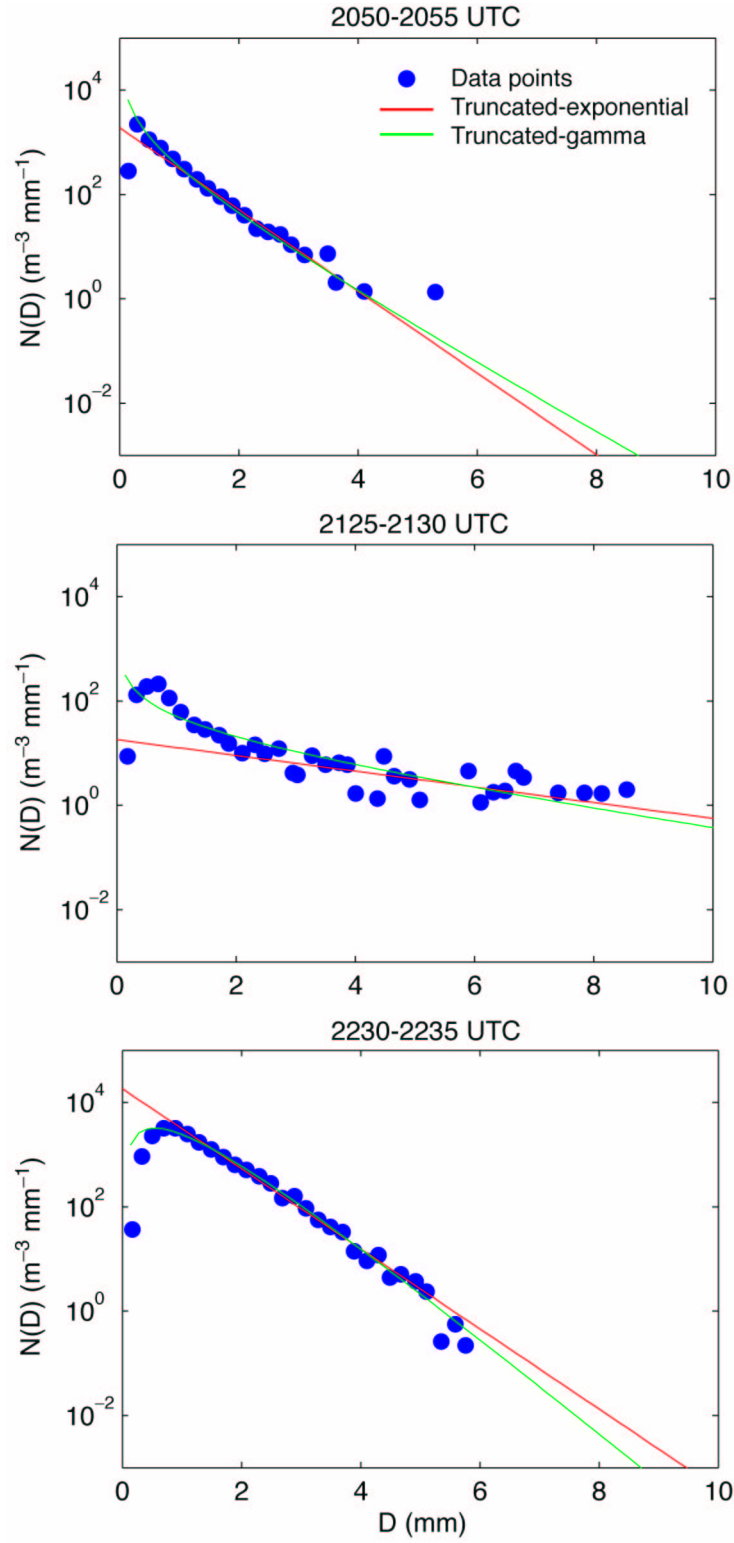
FIG. 3: Observed 5-min particle size distributions (number concentration plotted against equivalent diameter) for a long-lived snow event on 18 Mar 2003. Computed PSD properties are given in Table 1. Surface temperatures varied between 0°C and 0.3°C.
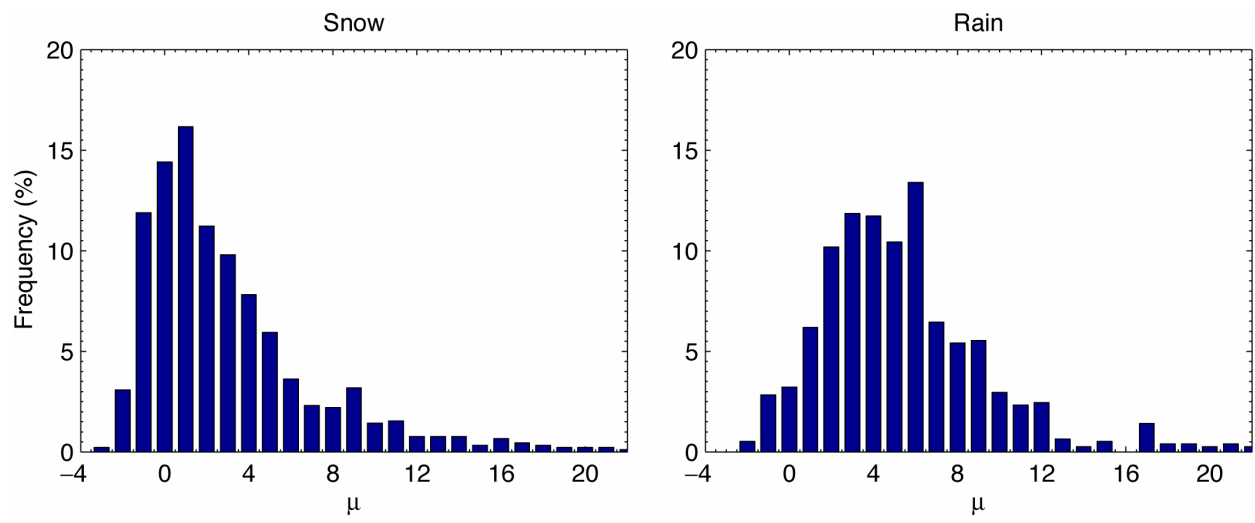
FIG. 4: Relative frequency of the truncated-gamma PSD shape factor μ for winter snow and rain storms. The total number of snow and rain spectra is 916 and 776, respectively.
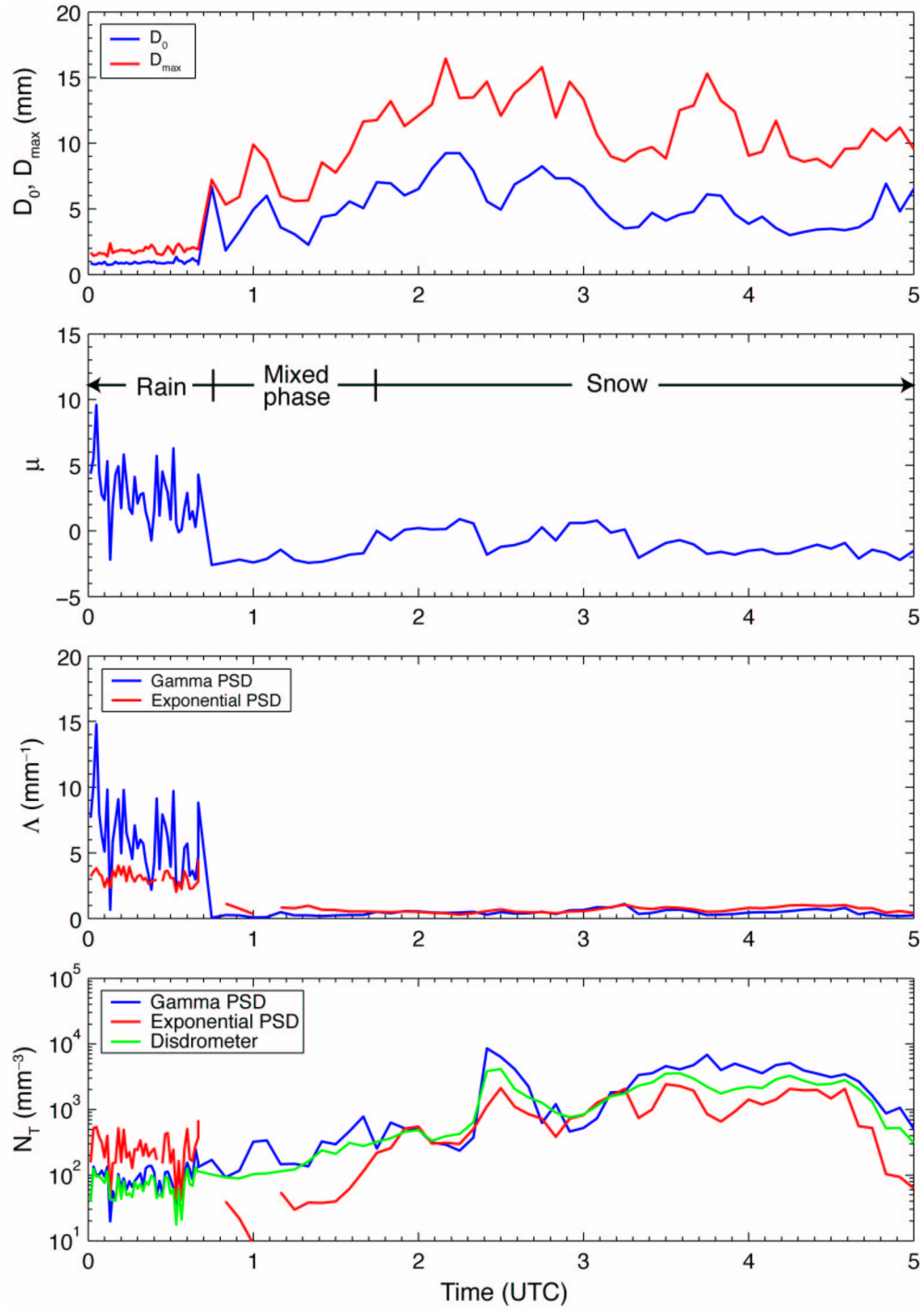
FIG. 5: Time series of PSD attributes for 1 Nov 2004 showing D_0 and D_{max}, the shape parameter μ for a truncated-gamma PSD, the slope parameter Λ for truncated-gamma and truncated exponential PSDs, and estimates of total concentration N_T.
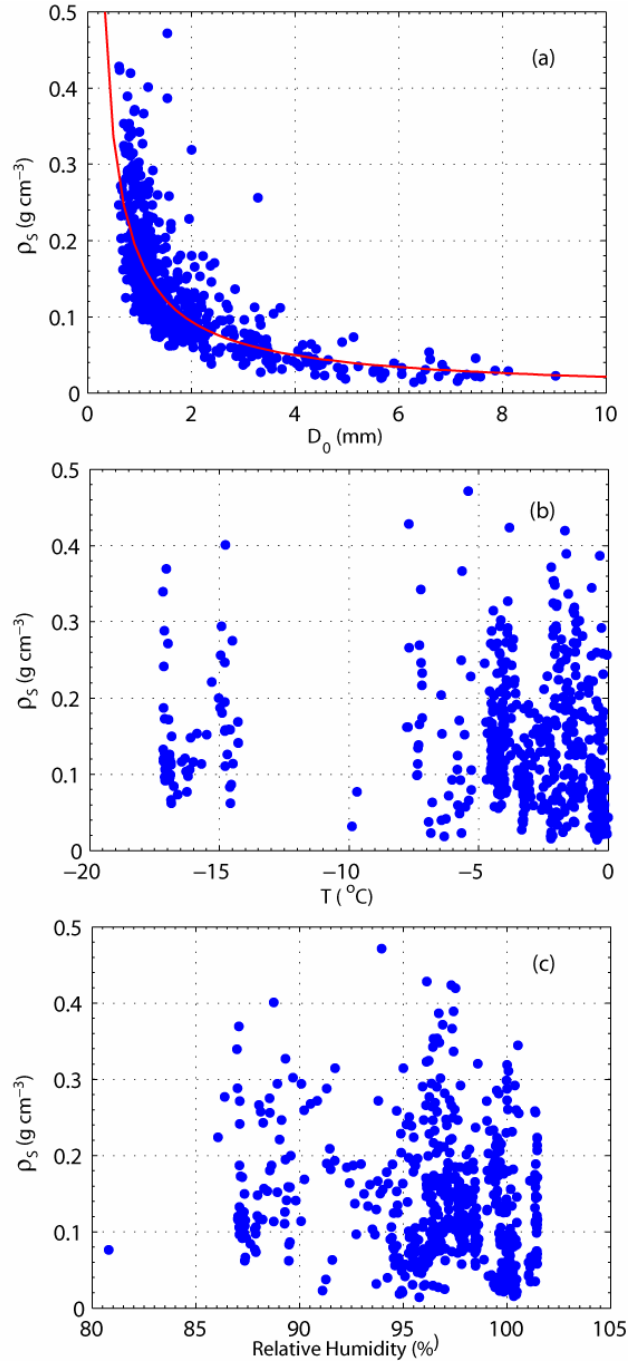
FIG. 6: Relationships between bulk density and (a) particle median volume diameter, (b) ambient temperature, and (c) relative humidity.
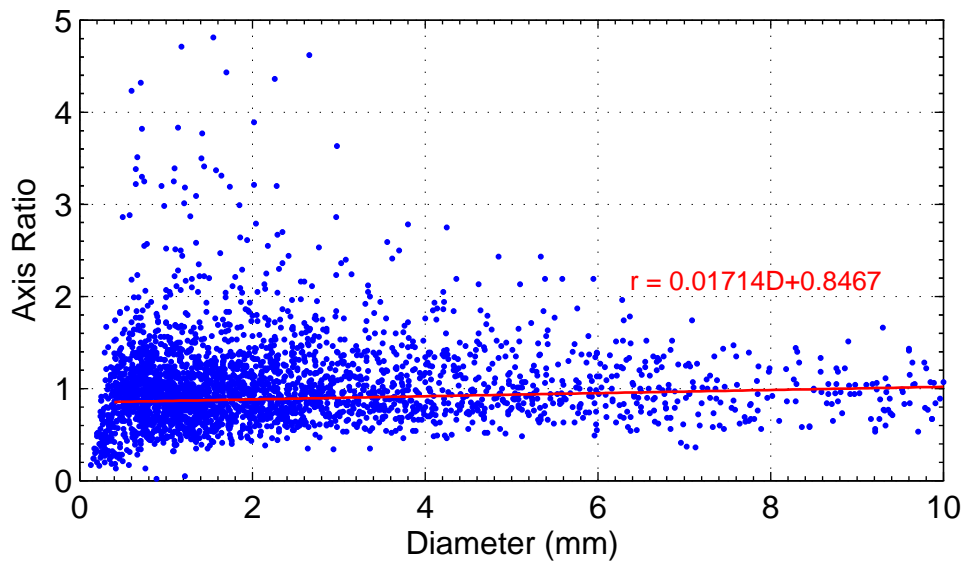
FIG. 7: Disdrometer axis ratios, maximum vertical dimension divided by the horizontal dimension. The red curve shows the modal shape of particles ≤ 10 mm. The data are from 0200 to 0220 UTC on 1 Nov 2004. Precipitation was dominated by irregular ice crystals and aggregates.
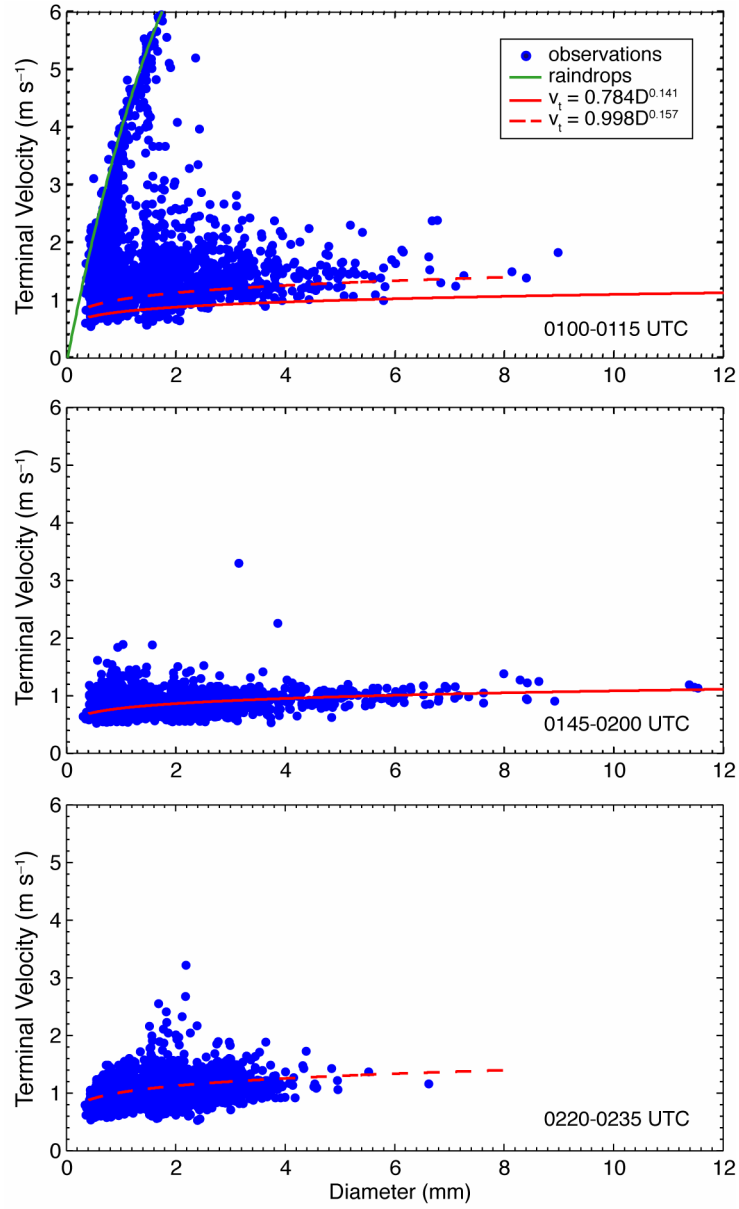
FIG. 8: Observed hydrometeor terminal velocities for three time periods in the storm of 5 Mar 2004. Fitted relations are overlaid. The raindrop relation is from Brandes et al. (2002).
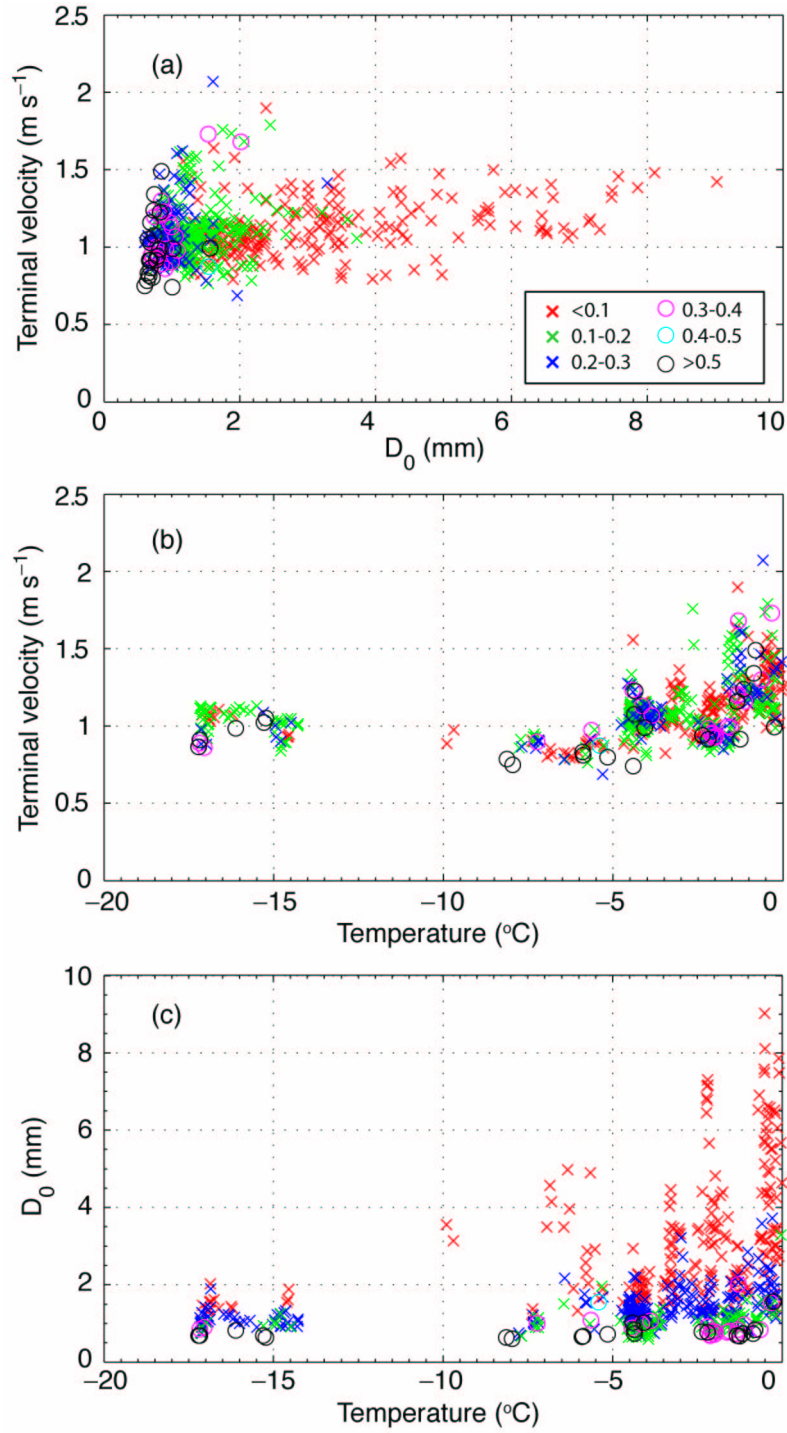
FIG. 9: Attributes of winter storm particle size distributions: (a) mass-weighted terminal velocity and median volume diameter, (b) terminal velocity and temperature, and (c) median volume diameter and temperature. Data points are color coded according to estimated density (panel a).
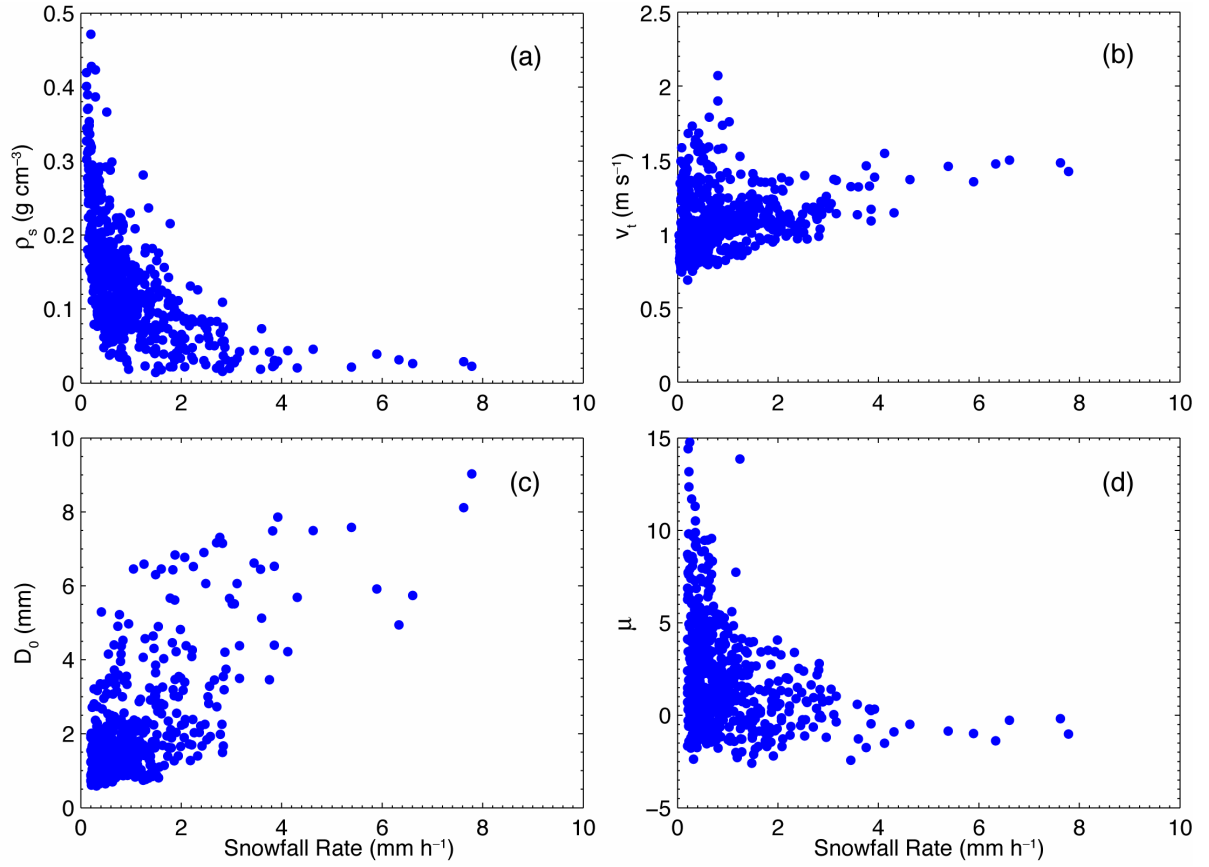
FIG. 10: Bulk snow density ρ_s, mass-weighted terminal velocity v_t, median volume diameter D_0, and the gamma PSD shape parameter μ plotted against snowfall rate expressed as liquid equivalent $(S > 0.2 \text{ mm h}^{-1})$.
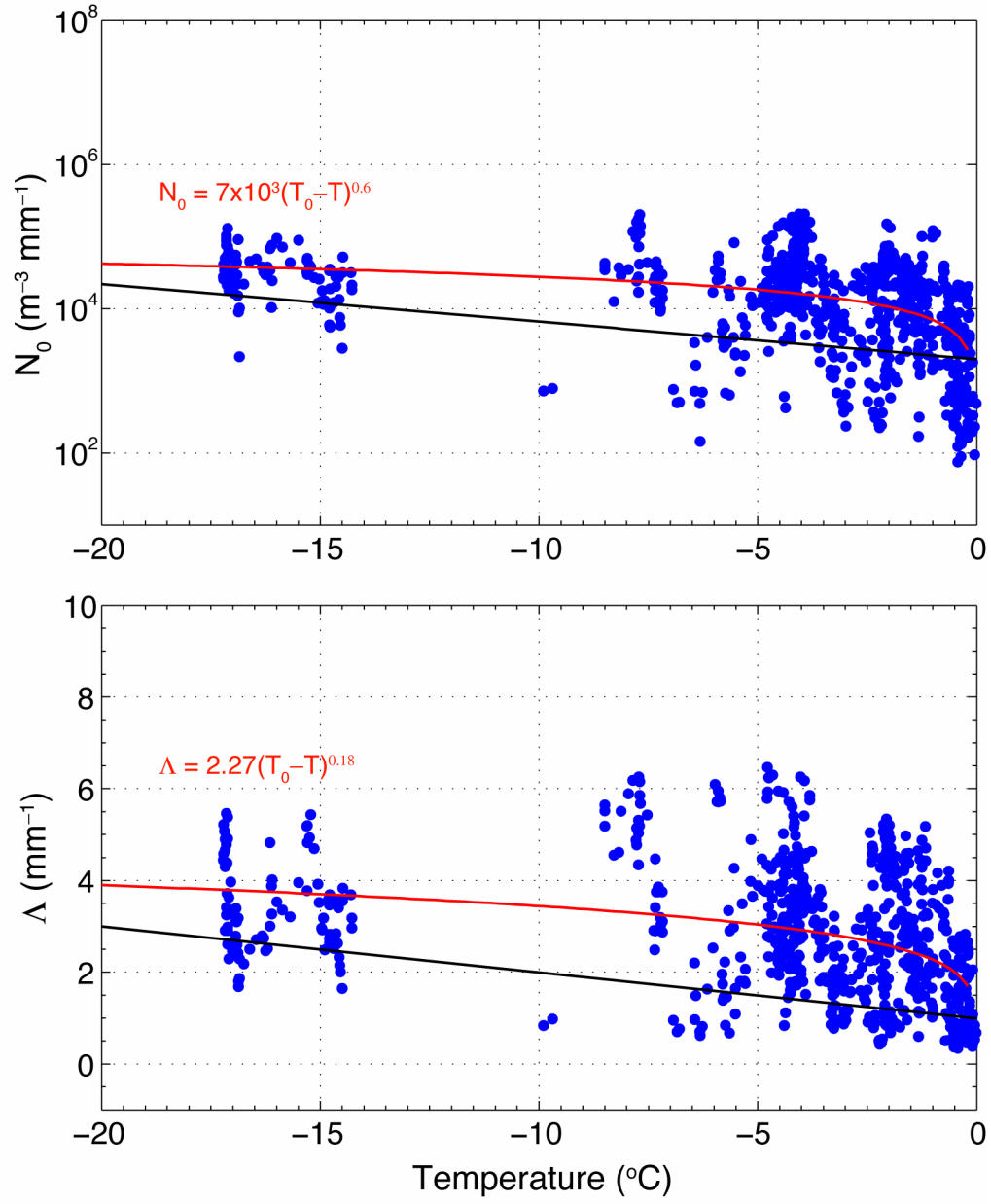
FIG. 11: Concentration and slope parameters for truncated-exponential PSDs plotted against surface air temperature. Relations fitted to the observations are in red; fits to the data of Houze et al. (1979) are in black.
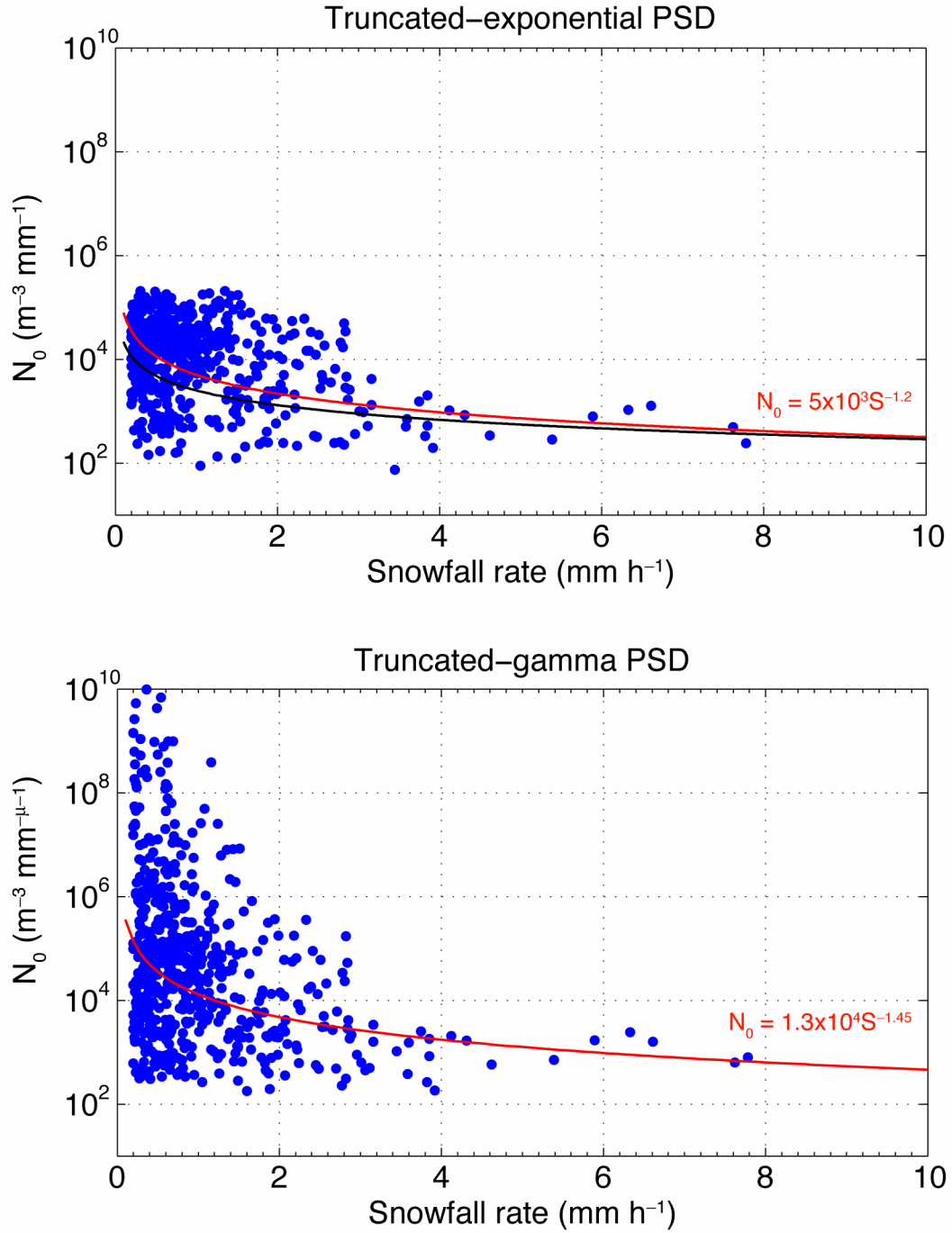
FIG. 12: The relationship between N_0 for truncated-exponential and truncated-gamma PSDs with snowfall rate. Relations fitted to the observations are shown in red. Equation (10) from Sekhon and Srivastava (1970), for an exponential PSD, is shown in black.
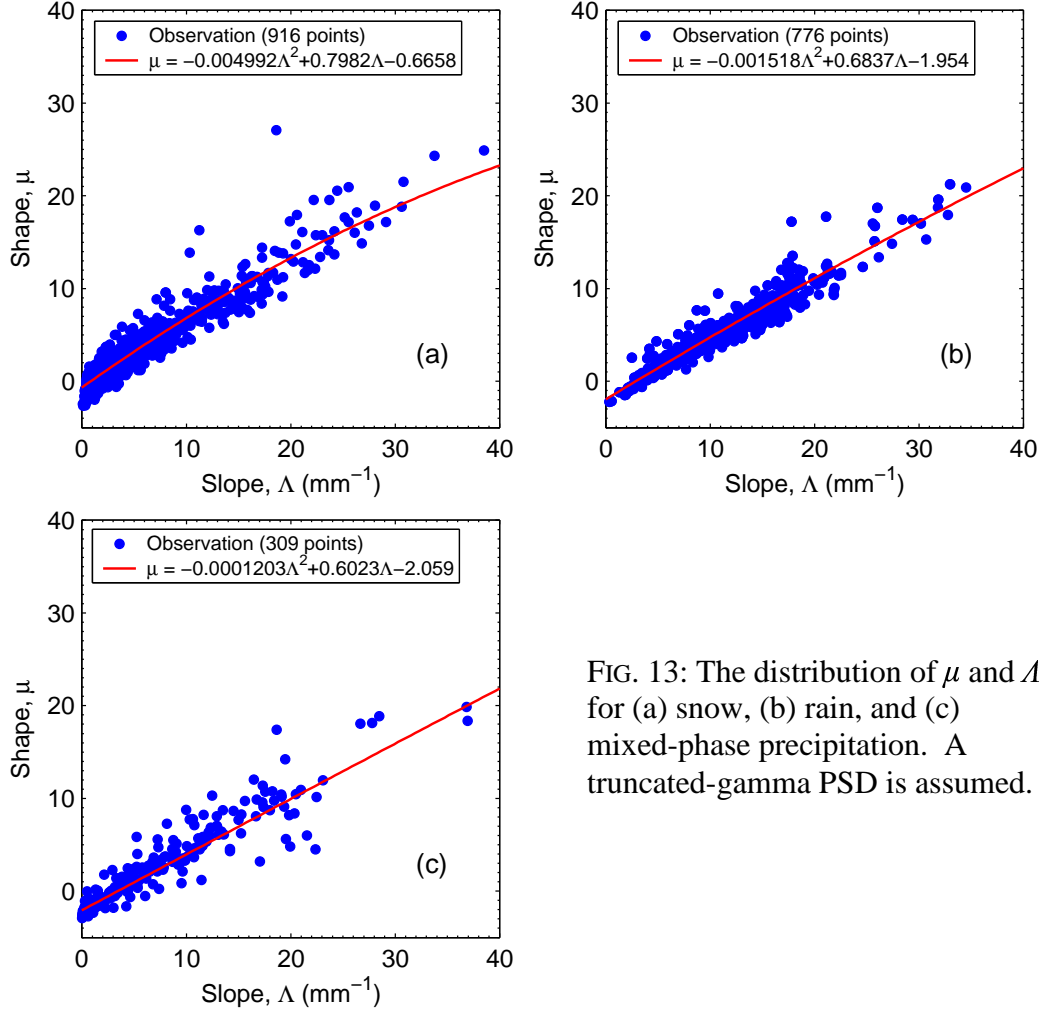
FIG. 13: The distribution of μ and Λ for (a) snow, (b) rain, and (c) mixed-phase precipitation. A truncated-gamma PSD is assumed.